Bidirectional Regulation of Motor Circuits Using Magnetogenetic Gene Therapy

Authors: Santiago R. Unda[1], Roberta Marongiu[1], Lisa E. Pomeranz[2], Jonathan P. Dyke[3], Edward K. Fung[3], Logan Grosenick[4], Rick Zirkel[5], Aldana M. Antoniazzi[1], Sofya Norman[1], Conor M. Liston[4], Chris Schaffer[5], Nozomi Nishimura[5], Sarah A. Stanley[6,7], Jeffrey M. Friedman[2], Michael G. Kaplitt[1*].

1. Laboratory of Molecular Neurosurgery, Department of Neurological Surgery, Weill Cornell Medical College, Cornell University; New York, NY, USA.
2. Laboratory of Molecular Genetics, Rockefeller University; New York, NY, USA.
3. Citigroup Bioimaging Center, Weill Cornell Medical College, Cornell University; New York, NY, USA.
4. Department of Psychiatry, Weill Cornell Medical College, Cornell University; New York, NY, USA.
5. Meining School of Biomedical Engineering, Cornell University, Ithaca, NY, USA.
6. Diabetes, Obesity and Metabolism Institute, Icahn School of Medicine at Mount Sinai, New York, NY, USA
7. Nash Family Department of Neuroscience and Friedman Brain Institute, Icahn School of Medicine at Mount Sinai, New York, NY, USA

***Corresponding author:** Michael G. Kaplitt (mik2002@med.cornell.edu)

Abstract

Regulating the activity of discrete neuronal populations in living mammals after delivery of modified ion channels can be used to map functional circuits and potentially treat neurological diseases. Here we report a novel suite of magnetogenetic tools, based on a single anti-ferritin nanobody-TRPV1 receptor fusion protein, which regulated neuronal activity in motor circuits when exposed to magnetic fields. AAV-mediated delivery of a cre-dependent nanobody-TRPV1 calcium channel into the striatum of adenosine 2a (A2a) receptor-cre driver mice led to restricted expression within D2 neurons, resulting in motor freezing when placed in a 3T MRI or adjacent to a transcranial magnetic stimulation (TMS) device. Functional imaging and fiber photometry both confirmed focal activation of the target region in response to the magnetic fields. Expression of the same construct in the striatum of wild-type mice along with a second injection of an AAVretro expressing cre into the globus pallidus led to similar circuit specificity and motor responses. Finally, a mutation was generated to gate chloride and inhibit neuronal activity. Expression of this variant in subthalamic nucleus (STN) projection neurons in PitX2-cre parkinsonian mice resulted in reduced local c-fos expression and a corresponding improvement in motor rotational behavior during magnetic field exposure. These data demonstrate that AAV delivery of magnetogenetic constructs can bidirectionally regulate activity of specific neuronal circuits non-invasively *in vivo* using clinically available devices for both preclinical analysis of circuit effects on behavior and potential human clinical translation.

40 **Introduction**

41 Neuromodulation has become a critical tool for both delineating functional brain circuits
42 underlying behaviors in animal studies and treating human patients with circuit disorders [1].
43 Electrical stimulation has long been used in pre-clinical studies and deep brain stimulation (DBS)
44 is a standard of care for patients with advanced tremors and Parkinson's disease (PD) [2]. Despite
45 the focal effects of electrical stimulation, the need for greater precision in modulating specific
46 circuits or neuronal populations has promoted the development of novel technologies.
47 Optogenetics combines viral delivery of light-sensitive ion channels with regulated light probes
48 for precise millisecond-time scale control of neural activity [3,4], but the microbial origin of the
49 channels and the need for a fiber optic implant can limit applications in animal studies and
50 provide challenges to human translation [5]. In contrast, chemogenetics delivers genes for
51 modified channels or receptors to allow drug-regulated control of neural activity without an
52 implant [6], but the response is dependent on drug diffusion to targeted regions and the time
53 course and longevity of responses rely on the pharmacokinetics of the drug.

54 Precise spatial and temporal control of neural circuitry without implanted devices could
55 be transformative for both pre-clinical studies and for human therapeutic applications [7]. *In vivo*
56 magnetic-field-based stimulation to control neural activity has shown promise in mammalian [5,7-
57 11] and non-mammalian systems [7,12]. Electromagnetic fields can penetrate tissue and transmit
58 energy to metal/metal oxide particles which in turn gate receptors and ion channels [13]. Taking
59 advantage of these properties, regulation of several brain structures has been achieved using
60 endogenous or genetically encoded members of the transient receptor potential cation channel
61 subfamily V (TRPV). Tethering of endogenous ferritin or external iron oxide nanoparticles (MNP)

62 [5 7,9] has been shown to lead to alternations of neural activity by magnetic fields *in vitro* and *in*
63 *vivo*. Previously the use of this system required the use of adenovirus vectors to deliver TRPV1
64 and ferritin cDNA clones which were too large for a single AAV vector.

65 Here, we report highly cell-specific, temporally precise, remote, and reversible
66 modulation of deep brain structures in awake, freely moving mice using a novel nanobody (Nb)
67 to endogenous ferritin (Ft) fused to the TRPV1 channel (Nb-Ft-TRPV1) encoded by a construct
68 packaged into a single AAV vector[14]. We show that cre-dependent magnetogenetic activation of
69 striatopallidal neurons elicits robust motor freezing in Adora-2a (A2a)-cre mice, similar to that
70 reported using opto- and chemogenetics [15-17]. The magnetic fields were delivered using standard
71 MRI machines or a commercially available Transcranial Magnetic Stimulation (TMS) device used
72 for human therapy, with a threshold of 180 mT to induce behavior alterations. Neural activation
73 was further confirmed using expression of *c-fos*, positron emission tomography (PET), and *in vivo*
74 fiber photometry to validate magnetogenetic-induced changes of neural activation. Circuit-
75 specific activation of striatopallidal neurons was also achieved in wild type (wt) mice using a
76 retrograde AAV encoding cre recombinase in combination with the cre-conditional
77 magnetogenetic construct. Finally, we achieved significant motor improvements in parkinsonian
78 mice using non-invasive, magnetogenetic inhibition of subthalamic nucleus (STN) neurons with a
79 nanobody-TRPV1 construct modified to block neuronal activity. The approach that is presented
80 provides for a means for inducing bidirectional, real-time regulation of neuronal circuits in freely
81 moving animals in a magnetic field and may have potential for a variety of human therapeutic
82 applications.

83 **Results**

84 **Magnetogenetic stimulation of striatal indirect pathway alters motor processing *in vivo.***

85 We targeted the indirect pathway *in vivo* using an AAV1/2 vector expressing an HA-tagged, cre-
86 dependent excitatory magnetogenetic Nb-Ft-TRPV1^{Ca2+} cassette flanked by a double floxed
87 inverted open reading frame (DIO) under the control of the JET promoter (AAV1/2-JET-DIO-Nb-
88 Ft-TRPV1^{Ca2+}-HA). The nanobody expressed from this construct has been shown previously to be
89 gated in the presence of a magnetic field via interactions between the anti-ferritin nanobody (Nb-
90 Ft) and endogenous ferritin with resulting neuronal activation, thus obviating the need for
91 delivering exogenous ferritin cDNAs[14].

92 The cre-dependent Nb-Ft-TRPV1^{Ca2+} AAV was injected bilaterally into the dorsal striatum
93 of transgenic mice expressing cre-recombinase in indirect spiny projection neurons (iSPN)
94 expressing dopamine type 2 (D2) receptors (A2a-cre mice) **(Fig. 1A upper panel)**. Immunostaining
95 for HA or RFP (for the AAV1/2-JET-DIO-mCherry control group) demonstrated efficient gene
96 expression in the dorsal striatum **(Fig. 1A lower panel)**. Histological analysis of transcript
97 expression using RNAScope confirmed that AAV transcripts co-localized only in D2 neurons **(Fig.
98 1B)**. To determine if this new magnetogenetic construct could functionally activate iSPNs *in vivo*,
99 we first examined motor activity after placing animals in a direct magnetic field (DMF) **(Fig 1C)**.
100 Parkinson's disease is associated with increased iSPN activity and optogenetic activation of these
101 neurons in normal mice results in rapid freezing [15]. Bilateral DMF stimulation (500 mT-1.3 T) using
102 a 3T MRI magnet significantly decreased activity compared to baseline, with activity returning to
103 normal after removal from the DMF **(Fig. 1D)**. There was also a marked increase in the time spent
104 freezing (n=10, 20.3 ± 2.8 vs 1.2 ± 0.69 sec, $p<0.001$), and a decrease of ambulation (n=10, 23.0

105 ± 5.1 vs 44.7 ± 1.9 sec, $p<0.001$) during DMF application in the Nb-Ft-TRPV1^{Ca2+} group placed in a
106 magnetic field compared to the mCherry group **(Fig. 1E & F)**.

107 To determine the threshold for magnetic field strength required to regulate striatal
108 cellular activity, we compared two different field gradients, 500 mT-1.3 T (High DMF titration)
109 **(Supplementary Fig. 1A)** and 100 mT-270 mT (Low DMF titration) as determined by placing a
110 gaussmeter in different locations in the cage at different distances from the 3T magnet **(Fig. 2A)**.
111 After mapping the magnetic field strength in the behavioral boxes **(Fig. 2B & Supplementary Fig.**
112 **1B)**, we then recorded the locomotor activity in animals expressing the magnetogenetic
113 construct. The activity heatmap in the presence of the Low DMF revealed a consistent decrease
114 of activity only when the mice receiving Nb-Ft-TRPV1^{Ca2+} were in proximal sections of the
115 behavior box with a field strength at or above 180 mT **(Fig. 2B)**. This contrasted with animals
116 exposed to the High DMF which showed reduced activity across the entire box **(Supplementary**
117 **Fig. 1C)**. Thus, while the freezing time was consistent throughout the box in the mice in the High
118 DMF titration **(Supplementary Fig. 1D)**, in the Low DMF titration there was a significant increase
119 in freezing time ($n=5$, $p<0.05$) only in the regions with >180 mT field strength **(Fig. 2B)**. This
120 threshold is consistent with a prior [10] report which used an earlier generation magnetogenetic
121 system consisting of separate TRPV1 and ferritin cDNAs to demonstrate that a DMF source of
122 ~0.2 T was sufficient to regulate deep brain circuits involved in food intake and glucose
123 homeostasis. To further evaluate whether a magnetic field gradient over 180 mT is sufficient to
124 induce a robust motor phenotype, we repeated our behavioral assessment at low DMF and high
125 DMF **(Fig. 2C)**. Consistent with the prior results, we found that mice expressing Nb-Ft-TRPV1^{Ca2+}
126 stayed at a relatively fixed location during both Low and High DMF application while control mice

127 expressing mCherry continued to move normally during DMF conditions **(Fig. 2 D & E)**. Indirect
128 pathway activation with both High and Low DMF application decreased the time spent
129 ambulating (n=5-8, p<0.001), and increased time spent freezing (n=5-8, p<0.001). **(Fig. 2 F & G)**.

130 **Magnetogenetic stimulation increases striatal neuronal activity *in vivo.***

131 We next assessed whether the changes in locomotor activity were correlated with changes in
132 neural activity. Previously the immediate early gene *c-fos* was shown to be increased in *vitro* and
133 *in vivo* in cells expressing TRPV1 and ferritin in a magnetic field [8,10,11]. Consistent with this, a
134 significantly higher proportion of striatal neurons expressing Nb-Ft-TRPV1^{Ca2+} showed c-*fos+*
135 expression compared to mCherry controls following exposure exposed to the MRI magnet (500
136 mT-1.3 T) (n=5, 23.65 ± 3.49 vs 5.79 ± 0.77 %, p<0.05) **(Fig. 3A & B)**. There was a correlation
137 between *c-fos* expression and freezing (n=4-5, Pearson's r=0.39, two-tailed n.s.) with the Nb-Ft-
138 TRPV1^{Ca2+} and mCherry mice clustering at opposite extremes of the correlation matrix **(Fig. 3C)**.
139 The data are consistent with there being a robust activation of the indirect pathway neurons,
140 with relatively low variability between the expression of gene activity-induced makers, and the
141 freezing phenotype.

142 To further assess striatal activity after magnetogenetic activation living animals, we used
143 positron emission tomography (PET) with [^{18}F] fluorodeoxyglucose (^{18}F-FDG), which measures
144 glucose utilization as a reflection of underlying neural activity [18]. Micro-PET-computed
145 tomography (CT) was performed in A2a mice expressing Nb-Ft-TRPV1^{Ca2+} fasted for 12 hrs. vs
146 mice receiving an mCherry in the striatum construct. ^{18}F-FDG was administered to the two groups
147 first without DMF exposure, followed 3 days later by PET imaging following the application of
148 DMF **(Fig. 3D upper panel)**. DMF exposure significantly increased striatal uptake of ^{18}F-FDG,

149 expressed as the ratio of uptake at baseline prior to DMF exposure to the magnetic field to the
150 signal after placement in a magnetic field. The ratio of the PET signal was significantly greater in
151 Nb-Ft-TRPV1^{Ca2+} group compared to mCherry controls (n=9-10, 1.14 ± 0.06 vs 0.98 ± 0.001,
152 p<0.05) **(Fig. 3D lower panel & E)**. To account for individual variability, we also quantified the
153 percentage of the ^{18}F-FDG dose that was injected dose gram (%ID/g) in the striatum compared
154 to uptake in cerebellum, with and without DMF treatment. DMF exposure significantly increased
155 ^{18}F-FDG uptake in the striatum in mice with Nb-Ft-TRPV1^{Ca2+} expression in D2 neurons relative to
156 mCherry controls (n=10, 1.37 ± 0.06 vs 1.19 ± 0.03 %ID/g, p<0.001) **(Fig. 3F)**. No change in the
157 PET signal was seen in cerebellum. Since clinically ^{18}F-FDG PET-CT is used to monitor Parkinson's
158 disease progression and can be correlated with motor features [18], we reasoned that the levels of
159 striatal glucose uptake might correlate with the time mice spent freezing during DMF application.
160 Consistent with this, the data showed a significant positive correlation (n=7-9, Pearson's r=0.69,
161 two-tailed p<0.05) between striatal glucose uptake and freezing time in the Nb-Ft-TRPV1^{Ca2+}
162 expressing mice **(Fig. 3G)**, with the most marked increase in the time spent freezing observed in
163 animals with a ^{18}F-FDG uptake over 1.4 using the cerebellum as a reference.

164 Finally, we used genetically encoded calcium indicators to measure magnetogenetic-
165 induced neural activity [5,7,11,12]. To selectively record D2 iSPN calcium transients during pre-DMF,
166 DMF, and post-DMF periods, we bilaterally injected a cre-dependent excitatory magnetogenetic
167 vector (AAV1/2-JET-DIO- Nb-Ft-TRPV1^{Ca2+} -HA) together with a cre-dependent calcium indicator
168 (AAV9-Syn-DIO-GCaMP6s) and implanted an optical fiber in the dorsal striatum of A2a-cre mice
169 **(Fig. 4A)**. This required the use of optical fibers that did not contain any metal which would heat
170 in the presence of a magnetic field. Nb-Ft-TRPV1^{Ca2+} expressing mice again showed motor

171 freezing in response to DMF that was correlated with an increased ΔF/F striatal GCaMP
172 fluorescence signal (**Fig. 4B)**, which was not seen in mCherry expressing mice **(Fig. 4D)**. Mean
173 GCaMP6 fluorescence (ΔF/F) percentage aligned to Pre-DMF, DMF, and Post-DMF revealed a
174 marked increase of fluorescence during DMF stimulation in the Nb-Ft-TRPV1^{Ca2+} group **(Fig. 4C)**
175 but not in the mCherry group **(Fig. 4E)**. Calcium transients in D2 iSPNs demonstrated by an
176 increase in GCaMP6 fluorescence (ΔF/F) were significantly increased by DMF treatment in the
177 Nb-Ft-TRPV1^{Ca2+} but not in the mCherry expressing mice (n=3-4, 27.91 ± 8.24 vs -1.37 ± 1.05%,
178 $p<0.05$) **(Fig. 4G)**. In parallel, DMF treatment significantly increased time spent freezing in Nb-Ft-
179 TRPV1^{Ca2+} compared to mCherry controls (n=3-4, $p<0.05$) confirming the functional efficacy of
180 magnetogenetic activation **(Fig. 4B & D)**. Consistent with the *c-fos* expression level and the PET
181 studies, there was a positive correlation between the change in fluorescent signal and the extent
182 of the motor inhibition (n=3-4, Pearson's r=0.60, two-tailed n.s.), with the experimental and
183 control groups mostly clustering at opposite ends of the correlation matrix **(Fig. 4H)**. This
184 combined data demonstrates that the fused ferritin nanobody-TRPV1 channel, expressed from a
185 single AAV in striatal D2 neurons, resulted in activation of transduced iSPNs which then caused
186 the resulting motor freezing.

187 **Transcranial magnetic stimulation (TMS) increases Nb-Ft-TRPV1^{Ca2+} mediated calcium**
188 **transients and elicits parkinsonian phenotype**.

189 While the MRI magnet was highly effective for demonstrating and characterizing the
190 magnetogenetic effect of the new construct on neurons within the brain, the feasibility of
191 translating into human application a technology which requires proximity to an MRI for
192 therapeutic efficacy is limited. To evaluate the potential of a more clinically relevant technology,

193 we repeated the studies above using a commercial transcranial magnetic stimulation (TMS)
194 system which is FDA approved for depression and other applications [19] **(Fig. 5A)**. Similar to the
195 effect of an MRI machine, TMS application at 20% output capacity using 50 twin pulses per
196 second with 1 second inter-stimulus intervals decreased motor ambulation in Nb-Ft-TRPV1^{Ca2+}
197 expressing mice compared with mCherry controls **(Fig. 5B)**. Analysis of motor parameters
198 including distance moved **(Fig. 5C & D)**, activity **(Supplementary Fig. 2A & B)**, and change of
199 location **(Supplementary Fig. 2D & E)** was consistent with activation of D2 iSPN in Nb-Ft-
200 TRPV1^{Ca2+} expressing mice compared to mCherry controls. Average distance moved and activity
201 percentage during TMS application was significantly decreased in the Nb-Ft-TRPV1^{Ca2+} expressing
202 mice (n=4-5, $p<0.05$) **(Fig. 5E, Supplementary Fig. 2C)**. Again, using targeted GCAMP expression
203 and fiber photometry, TMS treatment produced rapid generation of fluorescent positive spikes
204 in the striatum of Nb-Ft-TRPV1^{Ca2+} expressing mice while TMS treatment showed a sustained
205 decrease in GCaMP6 fluorescence in mCherry-expressing controls **(Fig. 5F & G)** [20]. Fluorescence
206 ($\Delta F/F$) quantification showed a significant increase in the Nb-Ft-TRPV1^{Ca2+} expressing mice
207 compared to their own baseline (n=3, 14.41 ± 4.15 vs -2.38 ± 0.81%, $p<0.05$) and compared with
208 mCherry mice during TMS application (n=3-4, 14.41 ± 4.15 vs -15.81 ± 5.61%, $p<0.05$) **(Fig. 5H)**.
209 These studies confirm that, as was seen with MRI generated magnetic fields, a clinically approved
210 TMS device is capable of activating transduced neurons and eliciting motor freezing in Nb-Ft-
211 TRPV1^{Ca2+} expressing mice at well below the maximal output of the device.

212 **Magnetogenetic stimulation of striatopallidal neurons in wild type mice reproduces a robust**
213 **motor phenotype.**

214 Cre-driver mouse lines provide cell specificity for functional mapping of neural circuits underlying
215 numerous behaviors and many diseases, but this approach is limited to animals. In addition,
216 expression is based on cellular identity and not on functional anatomical connections [21]. In order
217 to determine if magnetogenetics could be restricted to specific circuits in normal mice, we
218 utilized a dual vector system to restrict expression to the striatopallidal iSPN circuitry. AAV1/2-
219 JET-DIO-Nb-Ft-TRPV1^{Ca2+}-HA was first injected bilaterally into the dorsal striatum of normal mice,
220 which would not lead to expression of the viral transgene due to the absence of cre. This was
221 followed by a second injection of a retrograde AAV vector carrying a cre recombinase fused to
222 GFP (RetroAAV2-CMV-Cre-GFP) into the globus pallidus (Gp). This approach allows retrograde
223 uptake of AAV into afferents to the Gp, with resulting cre expression in neurons which project to
224 Gp, including D2 iSPNs. Since the only pallidal afferents containing a floxed transgene with this
225 approach would be those from the dorsal striatum, this should lead to restricted expression of
226 the magnetogenetic construct only in striatopallidal neurons. As expected, immunostaining for
227 HA or RFP (for AAV1/2-JET-DIO and the mCherry control group, respectively) demonstrated co-
228 localization of each with GFP from the transduced SPNs **(Fig. 6 A)**. The same behavioral tests were
229 then performed as were used to previously characterize the transgenic A2a-cre mice (**Fig.1**).
230 Consistent with the prior results, there was a robust decrease in locomotor activity when the
231 animals receiving the AAV1/2-JET-DIO-Nb-Ft-TRPV1^{Ca2+}-HA injections were placed in a magnetic
232 field compared to controls (**Fig. 6B)**. There was a significant decrease in ambulation during DMF
233 application (n=8, 16.13 ± 3.02 vs 39.38 ± 3.28 sec, $p<0.001$), and significant increase in time spent
234 freezing (n=8, 23.75 ± 4.63 vs 4.13 ± 1.34 sec, $p<0.001$) **(Fig. 6C & D)**. *c-fos* expression was again
235 significantly higher in the transduced iSPNs of Nb-Ft-TRPV1^{Ca2+} expressing mice compared to

236 mCherry controls (n=4, 26.34 ± 3.13 vs 10.76 ± 2.41 %, $p<0.001$) **(Fig. 6E & F).** To control for the
237 possibility that striatal overexpression of TRPV1 ion channels alone could mediate activation of
238 the indirect pathway in the absence of ferritin tethered to the TRPV1 channel, we compared the
239 effects of DMF treatment on wt mice expressing either Nb-Ft-TRPV1^{Ca2+} or TRPV1^{Ca2+} alone (**Fig.**
240 **6G)**. DMF application had no observable motor effect on TRPV1^{Ca2+} expressing mice but again
241 suppressed ambulation and increased freezing in mice expressing Nb-Ft-TRPV1^{Ca2+}, confirming
242 that fusion of the ferritin nanobody to the TRPV1 channel was required for neuronal activation
243 in the presence of a magnetic field **(Fig. 6H & I)**.

244 **Magnetogenetic inhibition of subthalamic nucleus neurons improves motor impairment in**
245 **parkinsonian mice.**

246 One advantage of chemogenetic and optogenetic systems is the availability of a suite of modified
247 channels which can inhibit neurons in addition to those which can activate neuronal firing [22].
248 Developing an inhibitory magnetogenetic system would not only expand the opportunities for
249 scientific research using this technology but would also provide translational opportunities for
250 diseases where neuronal inhibition would be desirable. We first validated *in vitro* the utility of
251 the anti-ferritin nanobody fused to a mutant TRPV1 channel modified to allow permeability of
252 Chloride (Cl-) ions (Nb-Ft-TRPV1^{Cl-}), which should increase chloride flux to inhibit neuronal activity
253 **(Fig. 7A)**. Neuro2A cells were transfected with plasmids expressing mCherry, TRPV1^{Ca2+} or Nb-Ft-
254 TRPV1^{Cl-} for fluorescent chloride imaging using MQAE, which is quenched by intracellular chloride
255 **(Supplementary Fig. 3A)**. Application of a low intensity magnetic field (MF, 230-250mT) showed
256 a significant decrease in the ΔF/F0 in the Nb-Ft-TRPV1^{Cl-} expressing cells compared to both
257 mCherry and TRPV1^{Ca2+} controls **(Fig. 7B)** (ΔF/F0 at 150s: Nb-Ft-TRPV^{Cl-} -0.16 ± 0.01,

258 TRPV1^{Ca2+}0.06 ± 0.01, mCherry -0.002 ± 0.01, p<0.001) consistent with increased intracellular
259 chloride concentrations.

260 The use of an inhibitory magnetogenetic system may be of potential use for symptomatic
261 treatment of Parkinson's disease (PD), where chemical or gene therapy-based inhibition of
262 subthalamic nucleus (STN) projection neurons can improve motor function in rodents, non-
263 human primates, and humans [23-27]. To test this, we generated unilateral 6-hydroxydopamine (6-
264 OHDA) lesions of nigral dopaminergic neurons in transgenic mice expressing the cre recombinase
265 in PitX-2-positive neurons (PitX-2-cre mice) **(Supplementary Fig. 3B)**, which restricts cre
266 expression to STN glutamatergic projection neurons with virtually no expression within other
267 populations in the vicinity [28]. Stable and functionally significant lesions were documented
268 through quantification of apomorphine-induced rotations, followed by randomization of animals
269 to balanced experimental and control groups and confirmation that DMF alone does not affect
270 rotations **(Supplementary Fig. 3C-D)**. A DIO cre-dependent AAV1/2 vector encoding the Nb-Ft-
271 TRPV1^{Cl-} cassette under the control of the JET promoter (AAV1/2-JET-DIO- Nb-Ft-TRPV1^{Cl-}-HA)
272 was then injected into the ipsilateral STN of 6OHDA-lesioned PitX2 mice, with another group
273 injected with a DIO cre-dependent mCherry vector as a negative control **(Fig. 7D)**. Mice
274 expressing Nb-Ft-TRPV1^{Cl-} in the STN showed a significant reduction of contralateral rotations
275 induced by the dopaminergic agonist, apomorphine, in the presence of a DMF application relative
276 to baseline and controls baseline (n=9-10, -46.62 ± 6.5 vs -2.67 ± 14.69%, p<0.05), **(Fig. 7E,**
277 **Supplementary Fig. 3E & F)**. The number of *c-fos* positive transduced neurons in the STN of PitX2-
278 cre mice was significantly decreased following DMF exposure in the group which received the
279 inhibitory magnetogenetic Nb-Ft-TRPV1^{Cl-}vector compared to mCherry controls **(Fig. 7F & G)**

280 (n=4, 15.01 ± 2.83 vs 48.89 ± 6.11%, $p<0.05$). This confirms that AAV-mediated expression of the
281 magnetogenetic inhibitory construct exclusively within PitX2-positive STN projection neurons
282 resulted in reduction of neuronal activity *in vivo* and a consequent improvement in motor
283 function following 6OHDA lesioning of the substantia nigra.

284 **Discussion**

285 The demonstration that viral vectors such as AAV can be used for gene transfer in the
286 mammalian brain [29] has transformed pre-clinical neuroscience research. Furthermore, many
287 completed and active clinical trials of gene therapy in humans have shown promise for treating
288 circuit disorders [27,30]. While initially genes cloned into AAV were expressed constitutively, more
289 recently techniques such as optogenetics and chemogenetics have been used to regulate neural
290 activity in an inducible manner, using light or drugs respectively. Optogenetics provides
291 temporally rapid and precise control of neuronal function but utilizes microbial-derived channels
292 that can be immunogenic and require permanent implantation of light-generating devices that
293 potentially tether small animals and present engineering and safety challenges for human
294 applications [4,31]. Chemogenetics uses drugs to regulate channels, which obviates the need for a
295 device implant, but chemogenetic regulation occurs in a more delayed fashion based upon the
296 pharmacokinetics of the activator molecules [32,33]. In this report, we validate magnetogenetics as
297 an alternative approach for modulating neural activity and show that magnetic field-based
298 regulation of neuronal function can be used for bidirectional control of neuronal activity. This
299 method provides both anatomical and temporal precision in awake, freely moving animals
300 without the need for an implanted device and uses a viral vector potentially applicable for clinical

301 studies and can respond to clinically approved devices which deliver sufficient strength magnetic
302 fields.

303 We validated this system using variants of TRPV1, which are endogenous mammalian
304 channels, together with a nano-body that binds to mouse and human ferritin[14]. We tested this
305 approach by eliciting a parkinsonian phenotype in freely moving mice to demonstrate the
306 functional efficacy of magnetogenetic activation of striatal indirect medium spinal neurons.
307 Activation of these neurons in a magnetic field was evident only in mice receiving the
308 magnetogenetic construct compared with controls, as confirmed by *c-fos* expression post-
309 mortem as well as both FDG-PET and fiber photometry in living animals. Optogenetic control of
310 basal ganglia circuitry has previously demonstrated similar changes in motor behavior after
311 selective activation of indirect pathways *in vivo* using an implanted light device to control neurons
312 expressing Channelrhodopsin-2 (ChR2) [15]. More recently, Munshi and colleagues [5] reported
313 successful magnetogenetic modulation of motor circuits targeting motor cortex and dorsal
314 striatum. Consistent with the classical model of basal ganglia circuitry, this study reported
315 decrease in voluntary movement by activation of striatal D2 iSPN using a combination of metal
316 nanoparticles (MNPs) and AAVs encoding TRPV1 channels stereotactically injected 4 weeks apart
317 in the ridge between dorsal and ventral striatum [5]. However, synthetic magnetic nanoparticles
318 would not allow for stable, chronic magnetogenetic activation and the use of MNPs could
319 potentially tether to other thermo-sensitive channels causing off target activation and safety
320 issues [7,34]. In addition, the intrinsic variability of separate injections and non-cell specific
321 transgene transduction can limit conclusions regarding the relationship between phenotype and
322 cells modulated by the exogenous particle-based magnetogenetic system. This is in contrast to

323 the genetically encoded system which we employed, which only requires injection of a single AAV
324 to improve both dosing consistency between subjects and longevity of neuromodulation due to
325 chronic AAV-mediated expression. For human translation, the ability to deliver a single construct
326 with a single infusion has both safety and regulatory advantages, and here we demonstrate the
327 viability of AAV-mediated delivery of a single magnetogenetic construct encoding a fused Nb
328 capable of tethering endogenous ferritin to an excitatory TRPV1 channel for inducible modulation
329 of neuronal activity leading to definable motor phenotypes.

330 The ability use of optogenetics, through a combination of focal delivery of viral constructs
331 expressing opsins and implantation of light emitting devices in a target brain region, has led to a
332 wealth of knowledge regarding the relevance of neuronal circuits to particular behaviors [35]. The
333 potential benefit of the magnetogenetic system described here is the use of a non-invasive
334 magnetic field to regulate specific circuits in freely moving animals, rather than a permanent
335 optical fiber implant which is tethered to an external device. We first demonstrated that a cre-
336 dependent magnetogenetic system can target particular neuronal populations in cre-driver mice.
337 However, this approach is limited to animals and may also not provide the anatomical specificity
338 required to examine anatomical circuits. To address this, we also developed a modified approach
339 combining delivery of the cre-dependent magnetogenetic activating construct into the striatum
340 with injection of a retrograde viral vector (AAVretro) into globus pallidus, a known target of
341 striatal iSPNs, to restrict expression of the activating construct exclusively within the same
342 striatopallidal iSPNs targeted in the A2a-cre driver mice. Histological analysis confirmed that
343 expression was restricted to striatal D2 neurons and the behavioral and physiological responses
344 to the magnetic field were similarly robust compared with data generated in the A2a-cre mice.

345 However, AAVretro may not efficiently transduce all neurons in a retrograde fashion and must
346 be individually tested for particular applications, though there are alternative retrograde viral
347 vectors that could also be used in such an approach if the pattern of retrograde uptake differs
348 between vectors [36]. Nonetheless, our data provide a novel means for non-invasive regulation of
349 specific neuronal circuits without the need for transgenic animals, which could not only be useful
350 for pre-clinical research but even have potential for circuit-specific human translation.

351 One potential limitation of the application of magnetogenetics in a clinical setting is the
352 availability of a device for generating a magnetic field that is suitable for human therapeutic
353 applications. Stanley and colleagues [10] previously reported successful bidirectional
354 magnetogenetic modulation of ventromedial hypothalamus (VMH) neurons using the earlier dual
355 construct system and an MRI to deliver the magnetic field, and we similarly observed a robust
356 motor phenotype following exposure to a 3T MRI in mice expressing Nb-Ft-TRPV1^{Ca2+} in iSPNs at
357 similar field strength thresholds. While this is feasible for experimental studies, any requirement
358 of proximity to a 3T MRI for efficacy could limit the translational potential of this technology. We
359 addressed this by also testing a TMS device as a source of AMF to induce magnetic-field-based
360 stimulation of D2 iSPNs. As with the MRI machine, we observed a sustained effect from the TMS
361 generated magnetic field in mice expressing Nb-Ft-TRPV1^{Ca2+} in striatal D2 iSPNs, with decreased
362 locomotion and corresponding increase in GCaMP fluorescence. Interestingly, *in vivo* fiber
363 photometry analysis also revealed that TMS reduced neural activity in control mice, which could
364 potentially be attributed to TMS frequency-dependent neural activation-inhibition. This is not
365 surprising, as TMS does influence neuronal activity in isolation, which is the basis for current
366 clinical applications. Human [37] and animal [20] reports that have shown suppression of neural

367 activity in motor-related regions with different protocols of TMS treatment, especially low-
368 frequency TMS. Nonetheless, this reduced activity had no behavioral effect and if anything
369 suggests that we may even have underestimated the magnitude of magnetogenetic neuronal
370 activation. Given the widespread and increasing use of TMS as a clinical device for non-invasive
371 neuromodulation in a variety of conditions [19], it is possible that magnetogenetics could be used
372 to either augment TMS or allow TMS to target deeper neuronal populations where the strength
373 of the magnetic field weakens but is still above the threshold that we have observed for
374 functional activation of the recombinant engineered channel. The ability to generate low field
375 strength at-home devices for intermittent modulation similar to TMS, while maintaining
376 anatomical specificity through focal delivery of the gene therapeutic, could also allow broader
377 application of this technology. Finally, the ability to regulate peripheral or autonomic neurons is
378 plausible using this technology for indications where either activation or inhibition of neural
379 activity is desirable, potentially including the control of pain, neuropathy symptoms or organ
380 function. Our data establishing the threshold for magnetic field strength also raises the possibility
381 that other more simple or even wearable magnetic devices may enable regulation of more
382 accessible neuronal populations.

383 To expand the utility of this system, we have also developed a novel construct with a
384 mutation that converted the sodium channel into a chloride channel, allowing magnetogenetic
385 inhibition of neuronal activity. Our *in vitro* data demonstrated the functionality of this new
386 construct, while AAV-mediated delivery of the construct to a population of glutamatergic
387 projection neurons within the STN of hemiparkinsonian PitX2-cre mice confirmed the *in vivo*
388 efficacy of magnetogenetic inhibition and consequent motor improvements in this setting. Pitx2

389 expression is restricted to neurons within the general region of the STN [38,39], allowing very limited
390 expression of our cre-conditional magnetogenetic system to this population of STN neurons.
391 Altered activity of the STN is widely believed to be one of the pathophysiological mechanisms
392 leading to PD motor deficits [40], hence traditional high frequency DBS in the STN has emerged as
393 a standard therapy for advance stages of PD [2]. Nonetheless, there is equipoise regarding the
394 mechanism of DBS action and the role of inhibition of STN neurons as a PD therapeutic. Gradinaru
395 and colleagues [40] found that optical inhibition of glutamatergic STN neurons in hemi-parkinsonian
396 rats was insufficient to affect motor behavior using early generation inhibitory opsins, yet STN
397 lesioning, infusion of GABA agonists into the STN and gene therapy to promote GABA production
398 within the STN have all demonstrated improved motor function in both pre-clinical studies and
399 human clinical trials [23-25,27,41]. While DBS may still function through mechanisms other than simple
400 neuronal inhibition [42], our results support a significant body of evidence suggesting that inhibition
401 of STN projection neurons can improve motor function in Parkinson's disease [23,27,43-46]. The
402 availability of an inhibitory magnetogenetic system, which can also be combined with retrograde
403 cre vectors to target specific populations and can be applied to peripheral neurons as well, could
404 vastly expand both the experimental and clinical potential of this technology.

405 In summary, the present study demonstrates that magnetogenetic gene therapy
406 efficiently regulates basal ganglia circuitry. A single AAV encoding the activating magnetogenetic
407 construct restricted to iSPNs elicited freezing phenotype in transgenic mice. Circuit-specific
408 magnetogenetic activation of iSPNs was replicated in wt mice using AAVretro to deliver cre to a
409 specific neuronal population, while expression of a novel inhibitory magnetogenetic construct
410 within the STN reduced activity with consequent motor improvement in hemiparkinsonian mice.

411 Our results provide a bidirectional toolkit for magnetogenetic regulation to study specific central
412 or peripheral neural circuits, while further development of the technology may facilitate
413 translation into amenable human conditions where non-invasive and immediate modulation of
414 neuronal activity could have therapeutic benefit.

415 **Materials and Methods**

416 ***Generation of AAV Constructs***

417 pAAV-JET-DIO-MCS/pLP362 is the backbone for the AAV vectors used to make **pAAV-JET-DIO-**
418 **mCherry, pAAV-JET-DIO-Nb-FT-TRPV1^{Ca2+}, pAAV-JET-DIO-Nb-Ft-TRPV1^{Cl-} and pAAV-JET-DIO-**
419 **TRPV1^{Ca2+}** and was made by replacing the BsrGI/NheI region of pAAV-hSyn-DIO-hM3D(Gq)-
420 mCherry (Addgene Cat No. 44361) with a multiple cloning site
421 (TGTACAACTAGTACCGGTTCGCGAGCATGCCCTAGGGCTAGC) and inserting a 242-bp PCR product
422 containing the JET promoter[47] amplified using primers 5'-
423 CTGCGGCCGCACGCGTGTACCATTGACGAATTCGGGCG and 5'-
424 ACTCTAGAGGATCCGGTACCTGTCAAGTGACGATCACAGGG into the MluI/KpnI sites.

425 To make **pAAV-JET-DIO-mCherry/**pLP388**,** the mCherry open reading frame was amplified using
426 primers 5'-ATTACCGGTGTTAACATGGTGAGCAAGGGCGAGGA
427 and 5'-TAAACCGGTCTTAAGTTACTTGTACAGCTCGTCCATG and cloned into AgeI-digested pAAV-
428 JET-DIO-MCS with the mCherry ORF in the reverse orientation to the JET promoter.

429 **pAAV-JET-DIO-Nb-FT-TRPV1^{Ca2+}/**pLP363 was made by ligating a 2943bp SpeI/EcoRV fragment
430 containing NbFT-TRPV1^{Ca2+} [14] to NruI/AvrII digested pAAV-JET-DIO-MCS.

431 The 865-bp HindIII/Tth111I fragment of pAAV-JET-DIO-Nb-FT-TRPV1^{Ca2+} was replaced with a 445-
432 bp HindIII-Tth111I fragment of synthesized DNA (Azenta Life Sciences, NJ) lacking the Nb-Ft
433 sequence to make **pAAV-JET-DIO-TRPV1^{Ca2+}**/pLP452**.**
434 To make **pAAV-JET-DIO-Nb-Ft-TRPV1^{Cl-}/**pLP375, primers 5'-
435 TCCATGGTGTTCTCCCTGGCAATGGGCTGGACCAACATGCTCT and
436 5'-AGACTAGTGTTATTTCTCCCCTGGGACCA were used to remove one NcoI site and amplify an
437 876-bp NcoI fragment of TRPV1^{mutant} encoding the I679K mutation[10] which was cloned into NcoI-
438 digested pAAV-JET-DIO-NbFT-TRPV1^{Ca2+}.
439 pAAV-CMV-Cre-GFP was obtained from Addgene Cat No. 68544.
440 ***Cell Culture and Adeno-Associated Virus (AAV) Preparation***
441 Human embryonic kidney (HEK293, ATCC #CRL-1573) cells were cultured in DMEM (Gibco),
442 supplemented with 10% (vol/vol) FBS (Sigma-Aldrich) and 1% (vol/vol) penicillin-streptomycin
443 (Gibco), at 37 °C in 95% humidified air and 5% CO2. Vector stocks were prepared by packaging
444 the plasmids into rgAAV2 or mixed serotype AAV1/2 particles using a calcium phosphate
445 transfection system as described previously[48]. Cells were harvested and lysed at 72 h after
446 transfection. The vectors were purified using iodixanol gradient and dialyzed against PBS with
447 2mM MgCl2. AAV titers were determined by qPCR using Syber Green chemistry and with primers
448 to the WPRE fragment of the AAV backbone.
449 ***Quantitative Real Time PCR (qPCR)***
450 To titer our purified viral vectors, AAV were processed as previously described[48] and viral
451 genomes quantified via qPCR using Fast SYBR green master mix (Applied Biosystems Cat. No
452 4385612) on the AB 7500 FAST Real Time PCR platform (Applied Biosystems) and primers to the

453 WPRE element: WPRE-Fw: 5’-GGCTGTTGGGCACTGACAAT-3’; WPRE-Rev: 5’-
454 CTTCTGCTACGTCCCTTCGG-3'. The relative number of full viral particles were calculated using the
455 standard curve method by normalizing to known standard samples.

456 ***Animals***

457 Male mice were housed two to five per cage and kept at 22°C on a reverse 11 am-light/11 pm-
458 dark cycle, with standard mouse chow and water provided ad libitum throughout the duration of
459 the study. All animal procedures were approved by the Institutional Animal Care and Use
460 Committee of Weill Cornell Medicine and were in accordance with National Institutes of Health
461 guidelines.

462 The following mice were used in these studies: i) wt C57BL/6J mice, obtained from Jackson
463 laboratory (Jax.org; strain #:000664); ii) 129S-Pitx2tm4(cre)Jfm/Mmucd (Pitx2-Cre; MMRRC stock
464 #:000126-UCD) and *B6.FVB(Cg)-Tg (Adora2a-cre) KG139Gsat/Mmucd* (A2a-Cre; MMRRC stock
465 #:036158-UCD).

466 ***Stereotactic Surgery***

467 All stereotactic surgical procedures were performed on 8–12-week-old mice, weighing 20g to
468 25g, under a mixture of ketamine/xylazine anesthesia. Ketamine (Butler Animal Health Supply)
469 and xylazine (Lloyd Laboratories) were administered at concentrations of 110 and 10 mg/kg body
470 weight i.p., respectively. After the induction of anesthesia, the animals were placed into a
471 stereotactic frame (David Kopf Instruments). All infusions were performed using a 10-µL
472 stereotactic syringe attached to a micro-infusion pump (World Precision Instruments) at a rate
473 of 0.1-0.4 µL/min. To prevent reflux, after each infusion, the injection needle was left in place for

474 5 min, withdrawn a short distance (0.3–0.5 mm), and then left in the new position for an
475 additional 2 min before removal. with a 33 G needle
476 To generate 6OHDA lesioned mice, animals were injected with a total volume of 0.6 µL of 6OHDA
477 hydrobromide (Sigma-Aldrich) in PBS with 0.1% ascorbate unilaterally into the medial forebrain
478 bundle (MFB) at a concentration of 2.5 mg/mL and an infusion rate of 0.1 µL/min with a 10-µL
479 Hamilton syringe with a 30 G needle. The coordinates for the injection were AP −1.1 mm, ML -
480 1.1 mm, DV −5.0 mm relative to bregma and the dural surface. Before lesion surgery, the
481 norepinephrine reuptake inhibitor desipramine (25 mg/kg, i.p.) was administered via i.p.
482 injection at least 30 min before 6OHDA infusion, to protect neostriatal and cerebellar
483 noradrenergic neurons from the toxin-induced damage. Mice were allowed 4-6-week recovery
484 before being subjected to the apomorphine-induced a behavioral test to estimate the extent of
485 dopamine depletion in the substantia nigra (see following section).
486 For experiments in Pitx2-cre mice, AAV1/2 vectors were injected into the subthalamic nucleus
487 (STN) unilateral to the lesioned side (AP -2.0 mm, ML -1.7 mm, DV −4.7 mm from bregma) of
488 6OHDA mice. For experiments in A2a-cre mice, AAV1/2 vectors were injected bilaterally into the
489 dorsal striatum (AP +0.5 mm, ML ±2.3 mm, DV −3.5 mm from bregma). For experiments in wt
490 mice, AAV1/2 vectors were injected bilaterally into the dorsal striatum (AP +0.5 mm, ML ±2.3
491 mm, DV −3.5 mm from bregma) and AAV2retro into the globus pallidus (AP +0.5 mm, ML ±2.3
492 mm, DV −3.5 mm from bregma). All craniotomies to inject AAV vectors were performed at a rate
493 of 0.4 µL /min using a 10-µL WPI syringe with a 33 G needle. A total of $2x10^{11}$ genomic particles/µL
494 (2 µL in PBS) of vectors were injected.

495 The mice were allowed a 6–8-week recovery before being subjected to the behavioral tests
496 during which maximal transgene expression from AAV vectors is achieved. At the conclusion of
497 the experiments, injection site accuracy within the targeted brain region was determined by
498 immunohistochemistry for the specific transgene expressed by the AAV vectors, and mice with
499 mistargeted injections were excluded from analysis before their data were unblinded.

500 **Sources of Magnetic field**

501 *Direct magnetic field (DMF)*

502 The magnetic field for *in vivo* studies was generated by the superconducting electromagnetic MRI
503 field from a Siemens 3.0 Tesla PRISMA MRI Scanner (Siemens Healthcare). The magnetic field
504 strength was measured and mapped using a gaussmeter (F.W. BELL MODEL 5080). High DMF was
505 defined as a region with a strength of 0.5-1.3 T, and Low DMF as 0.1-0.27 T.

506 *Transcranial magnetic stimulation (TMS)*

507 A butterfly C-B60 coil (165 x 85 x 19mm/inner diameter 35mm/outer diameter 75mm) was used
508 to deliver magnetic field during *in vivo* studies. Biphasic stimulation pulses were delivered by a
509 waveform generator (MagPro100x with MagOption) with the following settings: 20% machine
510 capacity (~600 mT), twin/dual mode 50 Hz stimulation, 500μs rise time, 1ms inter pulse interval,
511 10 pulses in train, number of trains 20, and inter train interval 1 s for 20 s.

512 ***Behavioral Assessments***

513 All behavioral tests were run during the dark phase of the mouse daily cycle. The experiments
514 were performed by an examiner blinded to treatment groups.

515 *Apomorphine induced rotations*

516 To test for 6OHDA lesion efficiency in Pitx2-cre mice, rotational behaviors were performed. In
517 brief, mice were placed in a body harness connected to a transducer/swivel in a bowl-shaped
518 testing arena (rotometer). Full 360° clockwise and counter-clockwise rotations were measured
519 over a 45-min period after drug injection for apomorphine-induced rotations. Apomorphine
520 (Sigma-Aldrich) was dissolved in saline solution, 0.9% NaCl, and 0.1% ascorbate, and
521 administered at a dose of 0.25 mg/Kg via s.c. injection. Mice we randomized based on the net
522 number of contralateral rotations before receiving STN injections of the inhibitory
523 magnetogenetic construct.
524 To test the effect of our AAV.Nb-Ft-TRPV1^{Cl-} vectors on inhibiting STN neuronal activity, rotational
525 behaviors were performed inside a 3T MRI room in a sound insulated, ventilated Styrofoam
526 chamber that contained a plastic arena of 26.5 x 26.5 x 26.5 cm. Video recordings of apomorphine
527 induced rotations were obtained beginning 10 minutes after 0.25 mg/Kg via s.c. injections for 5
528 minutes outside the magnetic field followed by 5 minutes inside the magnetic field [1.3T -
529 500mT], and another 5 minutes outside the magnetic field in the start position using a magnetic
530 field compatible camera (MRC HiSpeed camera, https://www.mrc-systems.de/en/products/mr-
531 compatible-cameras#12m-camera). Upon the conclusion of behavioral studies, nigral lesion
532 efficiency by 6OHDA was determined by immunohistochemistry for the tyrosine hydroxylase (TH)
533 protein as a marker for dopaminergic neurons in the substantia nigra. Mice with mistargeted
534 injections were excluded from analysis before their data were unblinded.
535 *Open-Field Arena*
536 Locomotor behavior in an open-field arena was performed inside a 3T MRI room using the same
537 chambers and video recording system as described above for apomorphine induced rotations.

538 For 2 days prior to testing, each mouse was habituated in the open field box for 10 minutes to
539 reduce any possible confounding effect of a new environment. On the day of testing, each mouse
540 was placed in the center of the open field, and spontaneous horizontal and vertical behaviors
541 were recorded during 5-min sessions of pre-DMF, during DMF, and post-DMF.

542 *Noldus EthoVision*

543 EthoVision XT14 was used to analyze offline rotational behaviors and open field videos. The
544 automatic animal detection with deep learning settings was used to track center to-nose and
545 center to-tail points in defined arenas. Video recordings were used to analyze the following
546 locomotion and rotational parameters: (1) distance travelled, (2) activity percentage (%), (3)
547 rotation >90 degrees clockwise, and counterclockwise. Tracking data and heatmaps were
548 graphed with EthoVision analysis tools.

549 *TRACKER*

550 TRACKER video analysis and modeling tool (TRACKER 6 free software,
551 https://physlets.org/tracker/) was used to track precise motor responses, including freezing and
552 ambulation time. Each second of the recordings was divided into 5 frames to track nose, center,
553 fore and hind paws, and tail every 2 frames resulting in 150 positions measured per minute.
554 Spatial motion in the Y axis, referred as "change of location", was also analyzed as a function of
555 time.

556 ***Immunohistochemistry***

557 On completion of all assessments, mice were deeply anesthetized with sodium pentobarbital
558 (150 mg/kg, i.p.) and transcardially perfused with 4% paraformaldehyde (PFA). Brains were
559 extracted and post-fixed overnight in 4% PFA, cryoprotected in 30% sucrose, and cut into 30-µm

560 sections using a vibratome (Leica Microsystems). Free-floating sections were treated with various
561 antibodies to visualize proteins of interest using immunofluorescence labeling, including tyrosine
562 hydroxylase (TH) to quantify the extent of nigral neurodegeneration, and mCherry or HA to
563 estimate the transduction efficiency from our AAV vectors. The following primary antibodies
564 were used: rabbit anti-RFP to detect mCherry (Rockland Cat. No 600-401-379; dil. 1:1000), sheep
565 anti-TH (Millipore Cat. No AB1542; dil. 1:1000), rabbit anti-HA (Sigma-Aldrich Cat. No H6908,
566 dil.1:500), and rat anti-cfos (Synaptic systems Cat. No 226-017, dil. 1:1000). Alexa Fluor-
567 conjugated fluorescent secondary antibodies (Molecular probes) were obtained from Life
568 Technologies and used at a 1:1000 dilution.

569 ***RNAScope in situ hybridization***

570 Thirty µm free floating brain sections were mounted in PBS onto charged Superfrost slides (Fisher
571 Scientific) and were allowed to air dry for ~ 2h. The experiments were performed as per
572 manufacturer's instructions (ACDbio). The incubations at 40°C and 60°C took place in the HybEZ
573 oven using the EZ-Batch system (ACDbio). Sections were first baked at 60°C for 1h and post-fixed
574 in 4% PFA for 15 min at 4°C. After the dehydration steps, slides were dried at 60°C for 15 min,
575 treated with hydrogen peroxidase (Cat No. 322335, ACDbio) at room temperature for 10 min,
576 and dried again at 60°C for 15 min before performing the retrieval step. Sections were incubated
577 in target retrieval buffer (Cat No. 322000, ACDbio) for 10 min at 100°C and washed two times
578 with double deionized water (ddH20). After 3 min incubation in 100% Ethanol and drying at 60°C
579 for 10 min, sections were then incubated in Protease III (Cat No. 322337, ACDbio) at 40°C for
580 30min, washed five times with ddH20, and incubated for 2h at 40°C with probes including Mm-
581 Drd2 – C1, Mm-Drd1 – C3, mCherry-C4. A slide for either positive and negative control probes

582 were also included (Cat No. 321811 and 321831 respectively, ACDbio). Two washes occurred in
583 between the following 40°C incubations with wash buffer (Cat No. 310091). Sections were
584 incubated for 30min with AMP1, 30 min with AMP2, and 15min with AMP3 (kit Cat No.323110).
585 Next, sections were incubated in HRP C1 for 15min and Opal 520 (1:1500; Cat No. OP-001001) in
586 TSA buffer (Cat No. 322809). Sections were next incubated in an HRP blocker for 15 min.
587 Following sections were incubated with HRP C2 in combination with Opal 650 (1:1500; Cat No.
588 OP-001003), and HRP C4 in combination with Opal 570 (1:1500; Cat No. OP-001005). Slides were
589 cover slipped with Prolong Gold containing DAPI (ACDbio).

590 ***PET/CT animal imaging studies***

591 All animal imaging experiments were performed in the Citigroup Biomedical Imaging Center
592 (CBIC, Weill Cornell Medicine). For baseline experiments, mice were fasted for 12 hours prior
593 imaging followed by. Intraperitoneal (i.p.) injection of ~500μCi ^{18}F-fluorodeoxyglucose (FDG), and
594 residual dose was measured. 1 hour after injection, mice were anesthetized with isoflurane and
595 scanned for 1 hour in a micro-PET/CT scanner (Siemens Inveon). For DMF experiments, mice were
596 exposed to a 3T MRI (DMF=500 mT – 1.3 T) for a total of 25 minutes after ^{18}F-FDG i.p.,
597 administration, and scanned following the same protocol as for baseline experiments. Following
598 imaging, scans were histogrammed and reconstructed using Siemens Inveon Acquisition
599 Workplace (Siemens Medical Solutions, Knoxville, TN, USA) and analyzed in DICOM format.
600 MRICron and MATLAB were used to do a PET-CT co-registration, and PMOD Fusion tool (version
601 3.6, PMOD Technologies Ltd., Zurich, Switzerland) was used for rigid transformations (manually
602 co-registered via rigid transformations [translations and rotations]), matching with MRI mouse
603 template, normalization with Mirrione mouse brain atlas, and regions of interest (ROI) analysis.

604 All analyses were conducted in a blinded fashion and were adjusted for mouse weight, ^{18}F-FDG
605 final dose (^{18}F-FDG$_{initial\ dose}$-^{18}F-FDG$_{residual\ dose}$), as well as relative to regions that do not express
606 dopamine 2-type receptors such as cerebellum. Right and left dorsal striatum were averaged for
607 each animal and MBq/ml or Percent injected dose per gram (%ID/g) were calculated to plot data.

608 ***In vivo fiber photometry***

609 Fiber photometry was performed to measure *in vivo* calcium dependent activity dynamics during
610 DMF/TMS stimulation. Cre-dependent AAVs expressing GCaMP6s (AAV9-Syn-DIO-GCaMP6s,
611 Addgene Cat. No 100845-AAV9) and Nb-Ft-TRPV1^{Ca2+}-HA/mCherry were injected bilaterally into
612 the dorsal striatum of A2a-Cre transgenic mice to restrict expression of GCaMP6s and NbFt-
613 TRPV1^{Ca2+}-HA or mCherry to D2 iSPNs. Two weeks following AAV injection, a 400-µm-diameter
614 optical fiber (Doric, MFC_400/430-0.48_5.5mm_ZF2.5(G)_FLT, Cat. No B280-4418-5) was
615 implanted in the dorsal striatum 0.5 mm above the AAV injection site (AP: +2.00mm, ML: −0.25
616 mm, DV: −2.15mm) and was secured with Metabond. Prior to behavioral testing, mice were
617 habituated for 2 days to a patch cord attached to the implanted optical fiber for 3 min sessions.
618 During behavioral testing, fiber photometry recordings were taken for 2 min before, during, and
619 post magnetic stimulation. Behaviors were performed and recorded using the same settings as
620 described above for open-field arena locomotor quantification. Following behavioral testing,
621 fluorescence microscopy was utilized to confirm GCaMP6s expression and optical fiber
622 placement. To excite GCaMP6s, light from a 470nm LED (Thorlabs, M470F3) modulated at a
623 frequency of 521Hz was passed through a filter (Semrock, FF02-472/30), reflected by a dichroic
624 (Semrock, FF495-Di03) and coupled to a 0.48 NA, 400µm core optical fiber patch cord (Doric).
625 Emitted fluorescence traveled back through the patch cord, passed through the dichroic, a filter

626 (Semrock, FF01-535/50), and was focused onto a photodetector (Newport, Model 2151). The
627 modulated signal passed from the photodetector to a RP2.1 real-time processor (Tucker Davis
628 Technologies) where it was demodulated, and low pass filtered using a corner frequency of 15Hz.
629 TTL pulses denoting the start of behavioral trials were passed to the processor in real time for
630 alignment of calcium recordings to behavioral measures.

631 ***In vitro chloride imaging***

632 Neuro 2A cells (ATCC ccl-131, mycoplasma testing and STR profiling performed by ATCC) were
633 grown in Eagles' minimum essential medium with 10% fetal bovine serum (Gibco) at 37°C and 5%
634 CO_2.

635 For immunocytochemistry studies, cells were cultured on 12-mm cover glass (Fisher Scientific,
636 Pittsburgh, PA) coated with fibronectin (Sigma). Cells were transfected with constructs
637 expressing Nb-Ft-TRPV1^{Cl-} or TRPV1^{Ca2+} 24 h after plating. Cells were stained 48-72hrs after
638 transfection.

639 For imaging studies using the chloride-dependent reporter MQAE, Neuro2A cells were grown on
640 12-mm cover glass and transfected with plasmids expressing mCherry alone, co-transfected with
641 NbFt-TRPV1^{Cl-} and mCherry or co-transfected with TRPV1^{Ca2+} and mCherry. Holotransferrin (2
642 mg/ml, Sigma) was added to cells 24 hours after transfection. Cells were placed at 32°C 24 hours
643 before imaging. Cells were washed 3 times with Krebs-HEPES buffer (NaCl 110 mM, KCl 5.5 mM,
644 $CaCl_2$ 2.5 mM, $MgCl_2$ 1.25 mM, HEPES 5mM and glucose 10mM) then incubated with MQAE 5mM
645 (Invitrogen) in Krebs-HEPES buffer for 1 hour at 37°C. Cells were then washed in Krebs-HEPES
646 buffer three times and placed in glass-bottom dishes with Krebs-HEPES buffer for 15 minutes
647 before imaging. Imaging was performed using an inverted fluorescent microscope Zeiss Axio

648 Observer Z1 microscope (Carl Zeiss, Oberkochen GER). Cells were imaged every 6 seconds for a
649 total of 3 mins with imaging before and during low AMF treatment with a neodymium magnet (K
650 and J magnetics) to produce a peak field 230-250mT. Image analysis was performed using FIJI.
651 Briefly, regions of interest (ROI) were selected based on mCherry expression and mean intensity
652 calculated for each ROI in each image after background subtraction. Chloride responses were
653 quantified as change in fluorescence intensity normalized to baseline fluorescence ($\Delta F/F0$).
654 Imaging was performed on at least three occasions for each condition and chloride responses
655 were measured in 142 cells (Nb-Ft-TRPV1^{Cl-}), 76 cells (TRPV1^{Ca2+}) and 181 cells (mCherry).
656 Immunocytochemistry (ICC) was used to confirm cell surface expression of TRPV1. Live cells were
657 incubated with rabbit anti-TRPV1 (extracellular) polyclonal antibody (Thermo Fisher Scientific
658 cat#PA5-77361) (1:50) in culture medium for 10 min at 37 °C followed by 5 washes with RT culture
659 medium. Cells were then incubated with goat anti-rabbit Alexa Fluor 633 (1:1000) for 10 min at
660 32 °C followed by a further 5 washes with RT culture medium. Cells were then fixed in 4%
661 paraformaldehyde in Hank's balanced salt solution (HBSS) for 30 min at room temperature and
662 washed 5 times in HBSS before mounting using Fluoromount with DAPI (Southern Biotech,
663 Birmingham, AL).

664 ***Imaging acquisition and analysis***

665 Images were taken by an epi-fluorescent microscope (Olympus BX61 microscope fluorescent
666 microscope fitted with an Olympus DP71 digital camera) or a confocal microscope (Zeiss LSM
667 900) and analyzed with Image J software (version 1.52p, NIH, US). For quantification of *c-fos*+
668 cells, coronal sections were sampled at intervals of 120-160μm for immunostaining. 3 dorsal
669 striatal or nigral sections per mouse were identified using the mouse brain atlas of Paxinos (2007)

670 and scanned bilaterally using a 20x objective. For each selected section, three randomly chosen
671 regions of interest (ROIs) with fixed areas were selected for quantification. A Macro Plugin was
672 applied to each section obtained, with a Gaussian blur filter threshold set to 30 and size filter to
673 20 to remove small objects and low signal cells. *c-fos*+ neurons were determined only when clear
674 co-localization with DAPI staining was observed. Automatized detection using Image J software
675 in 4-5 mice per condition (controls vs treated).

676 ***Statistics***

677 To make valid comparisons among experimental groups, mice were randomized based on
678 baseline motor behavior to achieve balanced, unbiased groups. Pitx2-cre mice were randomized
679 based upon contralateral rotational counts following systemic apomorphine injection (0.25
680 mg/Kg), measured at 4 weeks after 6OHDA lesion surgery. The sample size for our experiments
681 was determined by power analysis[49], published work in the field, and previous studies performed
682 by the PIs. Exact sample sizes for each experiment are indicated in figure legends. The power was
683 set at 95% probability, effect size to 0.3-0.5 depending on the experimental outcome, and
684 significance at $p<0.05$.

685 Statistical analyses were conducted using GraphPad Prism 7.0. The statistical test used in each
686 experiment depended on the type of data collected (reported in figure legends). We tested for
687 normality using the Kolmogorov-Smirnov test and Q-Q plots. Two-way ANOVA or two-tailed t test
688 for statistical comparisons were performed as appropriate.

689 For fiber photometry experiments, the change in fluorescent intensity ($\Delta F/F$) percentage was
690 calculated by subtracting the linear fit of the isosbestic signal to the raw GCaMP signal from the
691 raw GCaMP signal, median for the entire recording session was then subtracted from each

692 GCaMP event value and divided by the median; that is, (465_{raw} – 405_{fitted}) = 465_{net}; (465_{net} –

693 465_{median})/(465_{median}) x 100. Events were computed comparing means in pre-DMF/DMF/post-

694 DMF or baseline/TMS conditions.

695 Pearson's correlation coefficients were used to quantify associations between different readouts

696 (e.g., c-fos+ immunoreactivity vs freezing of gait). When comparing two sets of normally

697 distributed data, unpaired two-tailed t-tests were utilized.

698 **References**

699 1. Krauss JK, Lipsman N, Aziz T, et al. Technology of deep brain stimulation: current status
700 and future directions. *Nat Rev Neurol.* 2021;17(2):75-87.
701 2. Benabid AL, Chabardes S, Mitrofanis J, Pollak P. Deep brain stimulation of the subthalamic
702 nucleus for the treatment of Parkinson's disease. *Lancet Neurol.* 2009;8(1):67-81.
703 3. Boyden ES, Zhang F, Bamberg E, Nagel G, Deisseroth K. Millisecond-timescale, genetically
704 targeted optical control of neural activity. *Nat Neurosci.* 2005;8(9):1263-1268.
705 4. Deisseroth K. Optogenetics. *Nat Methods.* 2011;8(1):26-29.
706 5. Munshi R, Qadri SM, Zhang Q, Castellanos Rubio I, Del Pino P, Pralle A. Magnetothermal
707 genetic deep brain stimulation of motor behaviors in awake, freely moving mice. *Elife.*
708 2017;6.
709 6. Keifer O, Kambara K, Lau A, Makinson S, Bertrand D. Chemogenetics a robust approach to
710 pharmacology and gene therapy. *Biochem Pharmacol.* 2020;175:113889.
711 7. Wheeler MA, Smith CJ, Ottolini M, et al. Genetically targeted magnetic control of the
712 nervous system. *Nat Neurosci.* 2016;19(5):756-761.
713 8. Stanley SA, Gagner JE, Damanpour S, Yoshida M, Dordick JS, Friedman JM. Radio-wave
714 heating of iron oxide nanoparticles can regulate plasma glucose in mice. *Science.*
715 2012;336(6081):604-608.
716 9. Stanley SA, Sauer J, Kane RS, Dordick JS, Friedman JM. Remote regulation of glucose
717 homeostasis in mice using genetically encoded nanoparticles. *Nat Med.* 2015;21(1):92-
718 98.
719 10. Stanley SA, Kelly L, Latcha KN, et al. Bidirectional electromagnetic control of the
720 hypothalamus regulates feeding and metabolism. *Nature.* 2016;531(7596):647-650.
721 11. Chen R, Romero G, Christiansen MG, Mohr A, Anikeeva P. Wireless magnetothermal deep
722 brain stimulation. *Science.* 2015;347(6229):1477-1480.
723 12. Long X, Ye J, Zhao D, Zhang SJ. Magnetogenetics: remote non-invasive magnetic activation
724 of neuronal activity with a magnetoreceptor. *Sci Bull (Beijing).* 2015;60:2107-2119.
725 13. Stanley SA, Friedman JM. Electromagnetic Regulation of Cell Activity. *Cold Spring Harb*
726 *Perspect Med.* 2019;9(5).
727 14. Stanley SA, Pomeranz LE, Li R, et al. Magnetogenetic cell activation using endogenous
728 ferritin. *bioRxiv.* 2023:2023.2006.2020.545120.

729 15. Kravitz AV, Freeze BS, Parker PR, et al. Regulation of parkinsonian motor behaviours by
730 optogenetic control of basal ganglia circuitry. *Nature.* 2010;466(7306):622-626.
731 16. Yu C, Cassar IR, Sambangi J, Grill WM. Frequency-Specific Optogenetic Deep Brain
732 Stimulation of Subthalamic Nucleus Improves Parkinsonian Motor Behaviors. *J Neurosci.*
733 2020;40(22):4323-4334.
734 17. Alcacer C, Andreoli L, Sebastianutto I, Jakobsson J, Fieblinger T, Cenci MA. Chemogenetic
735 stimulation of striatal projection neurons modulates responses to Parkinson's disease
736 therapy. *J Clin Invest.* 2017;127(2):720-734.
737 18. Berti V, Pupi A, Mosconi L. PET/CT in diagnosis of movement disorders. *Ann N Y Acad Sci.*
738 2011;1228:93-108.
739 19. Cohen SL, Bikson M, Badran BW, George MS. A visual and narrative timeline of US FDA
740 milestones for Transcranial Magnetic Stimulation (TMS) devices. *Brain Stimul.*
741 2022;15(1):73-75.
742 20. Muller PA, Dhamne SC, Vahabzadeh-Hagh AM, Pascual-Leone A, Jensen FE, Rotenberg A.
743 Suppression of motor cortical excitability in anesthetized rats by low frequency repetitive
744 transcranial magnetic stimulation. *PLoS One.* 2014;9(3):e91065.
745 21. Harris JA, Hirokawa KE, Sorensen SA, et al. Anatomical characterization of Cre driver mice
746 for neural circuit mapping and manipulation. *Front Neural Circuits.* 2014;8:76.
747 22. Vlasov K, Van Dort CJ, Solt K. Optogenetics and Chemogenetics. *Methods Enzymol.*
748 2018;603:181-196.
749 23. Luo J, Kaplitt MG, Fitzsimons HL, et al. Subthalamic GAD gene therapy in a Parkinson's
750 disease rat model. *Science.* 2002;298(5592):425-429.
751 24. LeWitt PA, Rezai AR, Leehey MA, et al. AAV2-GAD gene therapy for advanced Parkinson's
752 disease: a double-blind, sham-surgery controlled, randomised trial. *Lancet Neurol.*
753 2011;10(4):309-319.
754 25. Kaplitt MG, Feigin A, Tang C, et al. Safety and tolerability of gene therapy with an adeno-
755 associated virus (AAV) borne GAD gene for Parkinson's disease: an open label, phase I
756 trial. *Lancet.* 2007;369(9579):2097-2105.
757 26. Hasegawa T, Chiken S, Kobayashi K, Nambu A. Subthalamic nucleus stabilizes movements
758 by reducing neural spike variability in monkey basal ganglia. *Nat Commun.*
759 2022;13(1):2233.
760 27. Niethammer M, Tang CC, LeWitt PA, et al. Long-term follow-up of a randomized AAV2-
761 GAD gene therapy trial for Parkinson's disease. *JCI Insight.* 2017;2(7):e90133.
762 28. Guillaumin A, Pietro Serra G, Georges F, Wallén-Mackenzie Å. Optogenetic investigation
763 into the role of the subthalamic nucleus in motor control. *bioRxiv.* 2020.
764 29. Kaplitt MG, Leone P, Samulski RJ, et al. Long-term gene expression and phenotypic
765 correction using adeno-associated virus vectors in the mammalian brain. *Nat Genet.*
766 1994;8(2):148-154.
767 30. Deverman BE, Ravina BM, Bankiewicz KS, Paul SM, Sah DWY. Gene therapy for
768 neurological disorders: progress and prospects. *Nat Rev Drug Discov.* 2018;17(10):767.
769 31. Shen Y, Campbell RE, Cote DC, Paquet ME. Challenges for Therapeutic Applications of
770 Opsin-Based Optogenetic Tools in Humans. *Front Neural Circuits.* 2020;14:41.
771 32. Poth KM, Texakalidis P, Boulis NM. Chemogenetics: Beyond Lesions and Electrodes.
772 *Neurosurgery.* 2021;89(2):185-195.

773 33. Jendryka M, Palchaudhuri M, Ursu D, et al. Pharmacokinetic and pharmacodynamic
774 actions of clozapine-N-oxide, clozapine, and compound 21 in DREADD-based
775 chemogenetics in mice. *Sci Rep.* 2019;9(1):4522.
776 34. Hernandez-Morales M, Han V, Kramer RH, Liu C. Evaluating methods and protocols of
777 ferritin-based magnetogenetics. *iScience.* 2021;24(10):103094.
778 35. Tye KM, Deisseroth K. Optogenetic investigation of neural circuits underlying brain
779 disease in animal models. *Nat Rev Neurosci.* 2012;13(4):251-266.
780 36. Sarno E, Robison AJ. Emerging role of viral vectors for circuit-specific gene interrogation
781 and manipulation in rodent brain. *Pharmacol Biochem Behav.* 2018;174:2-8.
782 37. Wang WC, Wing EA, Murphy DLK, et al. Excitatory TMS modulates memory
783 representations. *Cogn Neurosci.* 2018;9(3-4):151-166.
784 38. Parolari L, Schneeberger M, Heintz N, Friedman JM. Functional analysis of distinct
785 populations of subthalamic nucleus neurons on Parkinson's disease and OCD-like
786 behaviors in mice. *Mol Psychiatry.* 2021;26(11):7029-7046.
787 39. Wallen-Mackenzie A, Dumas S, Papathanou M, et al. Spatio-molecular domains identified
788 in the mouse subthalamic nucleus and neighboring glutamatergic and GABAergic brain
789 structures. *Commun Biol.* 2020;3(1):338.
790 40. Gradinaru V, Mogri M, Thompson KR, Henderson JM, Deisseroth K. Optical deconstruction
791 of parkinsonian neural circuitry. *Science.* 2009;324(5925):354-359.
792 41. During MJ, Kaplitt MG, Stern MB, Eidelberg D. Subthalamic GAD gene transfer in
793 Parkinson disease patients who are candidates for deep brain stimulation. *Hum Gene*
794 *Ther.* 2001;12(12):1589-1591.
795 42. Ashkan K, Rogers P, Bergman H, Ughratdar I. Insights into the mechanisms of deep brain
796 stimulation. *Nat Rev Neurol.* 2017;13(9):548-554.
797 43. Ricardo Y, Pavon N, Alvarez L, et al. Long-term effect of unilateral subthalamotomy for
798 Parkinson's disease. *J Neurol Neurosurg Psychiatry.* 2019;90(12):1380-1381.
799 44. Martinez-Fernandez R, Manez-Miro JU, Rodriguez-Rojas R, et al. Randomized Trial of
800 Focused Ultrasound Subthalamotomy for Parkinson's Disease. *N Engl J Med.*
801 2020;383(26):2501-2513.
802 45. Ji YW, Zhang X, Fan JP, et al. Differential remodeling of subthalamic projections to basal
803 ganglia output nuclei and locomotor deficits in 6-OHDA-induced hemiparkinsonian mice.
804 *Cell Rep.* 2023;42(3):112178.
805 46. Milosevic L, Kalia SK, Hodaie M, Lozano A, Popovic MR, Hutchison W. Subthalamic
806 suppression defines therapeutic threshold of deep brain stimulation in Parkinson's
807 disease. *J Neurol Neurosurg Psychiatry.* 2019;90(10):1105-1108.
808 47. Tornoe J, Kusk P, Johansen TE, Jensen PR. Generation of a synthetic mammalian promoter
809 library by modification of sequences spacing transcription factor binding sites. *Gene.*
810 2002;297(1-2):21-32.
811 48. Morgenstern PF, Marongiu R, Musatov SA, Kaplitt MG. Adeno-associated viral gene
812 delivery in neurodegenerative disease. *Methods Mol Biol.* 2011;793:443-455.
813 49. Charan J, Kantharia ND. How to calculate sample size in animal studies? *J Pharmacol*
814 *Pharmacother.* 2013;4(4):303-306.
815

Acknowledgments

This study was supported by the National Institute of Health R01 NS097184 (JMF, MGK) and the JPB Foundation (JMF, MGK).

We acknowledge Henning U. Voss and Immanuel Elbau for assistance with the video-recording systems during MRI and TMS, William Tower for assistance with the EthoVision software, Neranjan de Silva for assistance breeding mice, Violetta Manusajyan for technical support during MRI recordings, Leah Kelly for helpful discussions during experiments and Muc Chieu Du and Kamaar Lawson for assistance with use of the Citigroup Biomedical Imaging Center.

Author contributions:

Conceptualization: JMF, MGK

Methodology: SRU, RM, JMF, MGK

Investigation: SRU, RM, LEP, AMA, SN, JPD, EKF, LG, RZ, SAS, MGK

Visualization: JMF, MGK.

Funding acquisition: MGK, JMF

Supervision: JMF, MGK

Writing – original draft: SRU, MGK

Writing – review & editing: SAS, JMF, MGK

Competing interest:

The authors declare no competing interests.

Materials & Correspondence:

Michael G. Kaplitt (mik2002@med.cornell.edu)

Figures

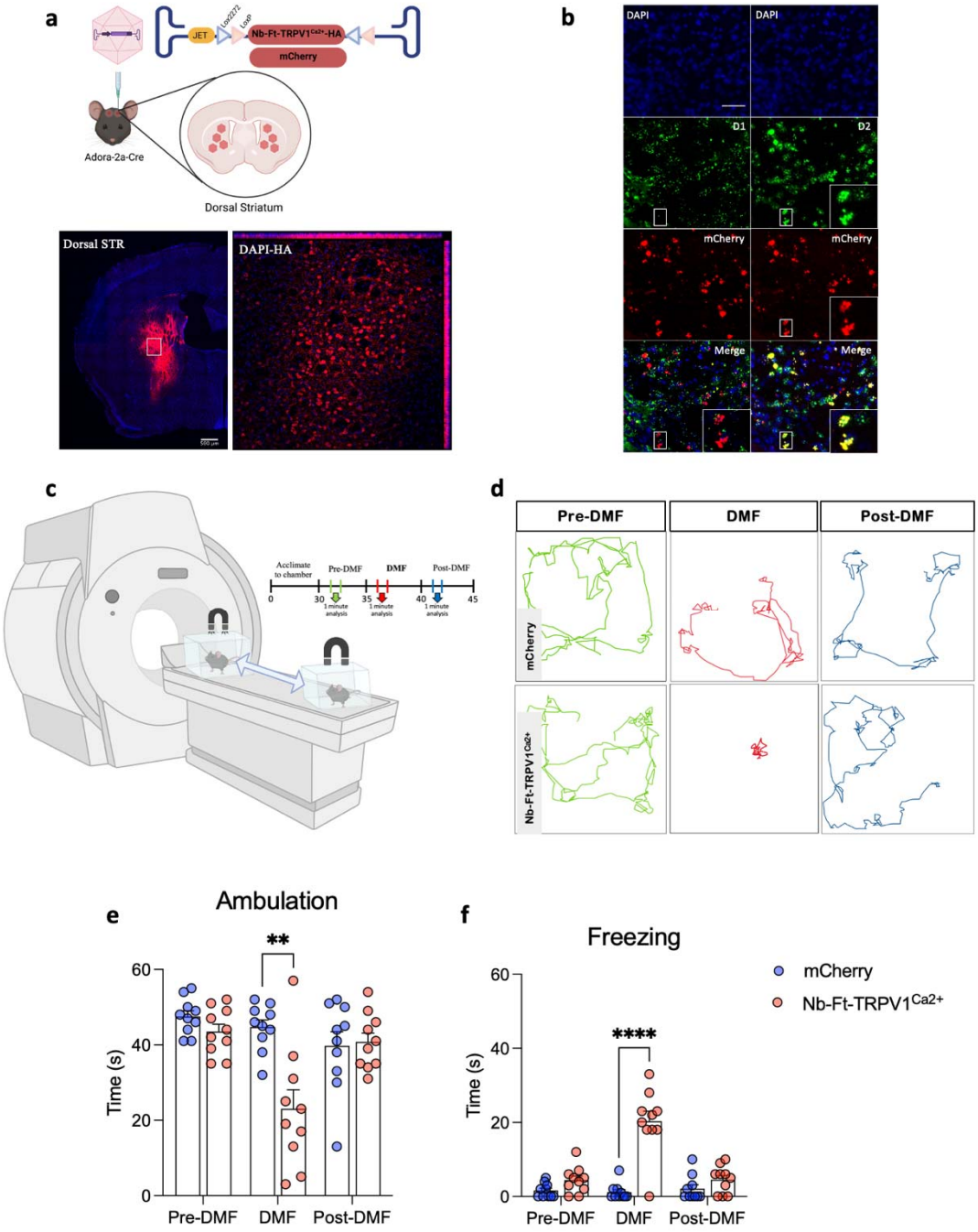

Fig. 1. Selective viral-mediated expression of Nb-Ft-TRVP1^{Ca2+} in striatal iSPNs elicit parkinsonian motor behavior. a. Schema of the double-floxed Cre-dependent AAV vector expressing the Nb-Ft-TRVP1^{Ca2+} or mCherry under the control of the JET promoter, and

immunostaining for HA in Adora-2A (A2a)-Cre mice demonstrates selective expression of the AAV- Nb-Ft-TRVP1^{Ca2+} in dorsal striatum. **b.** Selective transduction of D2-type iSPN with RNA in-situ hybridization (ISH). Co-localization of D2-type (green) iSPN with mCherry (red). **c.** Protocol and Schema for direct magnetic field (DMF) neural activation to assess motor behavior. **d.** Example of altered motor activity during bilateral striatal pre-DMF (green), DMF (red) and post-DMF (blue) stimulation; individual lines represent the path of a single mouse. Effect of DMF stimulation on **e.** Ambulation bout duration, and **f.** Freezing of gait in mCherry (blue bars/dots, n=10) and Nb-Ft-TRVP1^{Ca2+} (red bars/dots, n=10) mice. Error bars show SEM. ** represents p value < 0.001 with Student's t test.

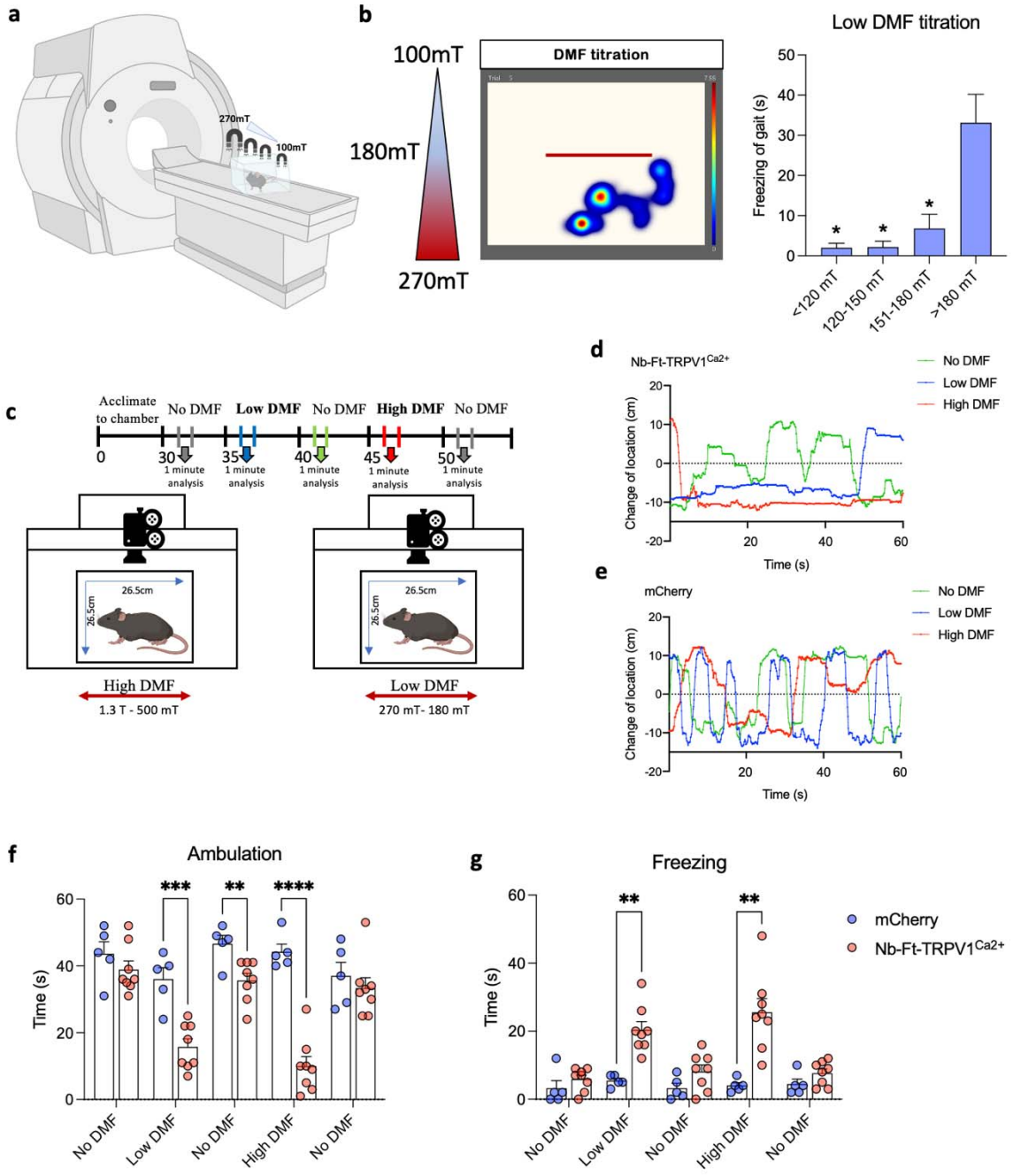

Fig. 2. Nb-Ft-TRPV1^{Ca2+} in D2 iSPNs stimulated with high DMF and low DMF treatment produce freezing of gait. a. Schema for low direct magnetic field (DMF) titration. **b.** Magnetic field strength and individual activity heatmap example of motor activity during bilateral striatal Low DMF titration in Nb-Ft-TRPV1^{Ca2+} expressing mice. Freezing of gait in different magnetic

field gradients in the Low DMF titration ranges (blue bars, n=5) in Nb-Ft-TRPV1^{Ca2+} expressing mice. **c.** Protocol and schema for High DMF and Low DMF stimulation in A2a-Cre mice injected with the double-floxed Cre-dependent AAV vector expressing the Nb-Ft-TRPV1^{Ca2+} or mCherry under the control of the JET promoter. Representative tracking data of change of location in **d.** Nb-Ft-TRPV1^{Ca2+} and **e.** mCherry A2a-Cre mice during High DMF (red line), Low DMF (blue line), and No DMF (green line) treatment. Effect of High DMF and Low DMF stimulation on **f.** Ambulation and **g.** Freezing of gait in Nb-Ft-TRPV1^{Ca2+} (red dot/bars, n= 8) and mCherry (blue dots/bars, n=5). Error bars show SEM. * represents p value < 0.05, ** represents p value < 0.001 with Student's t test.

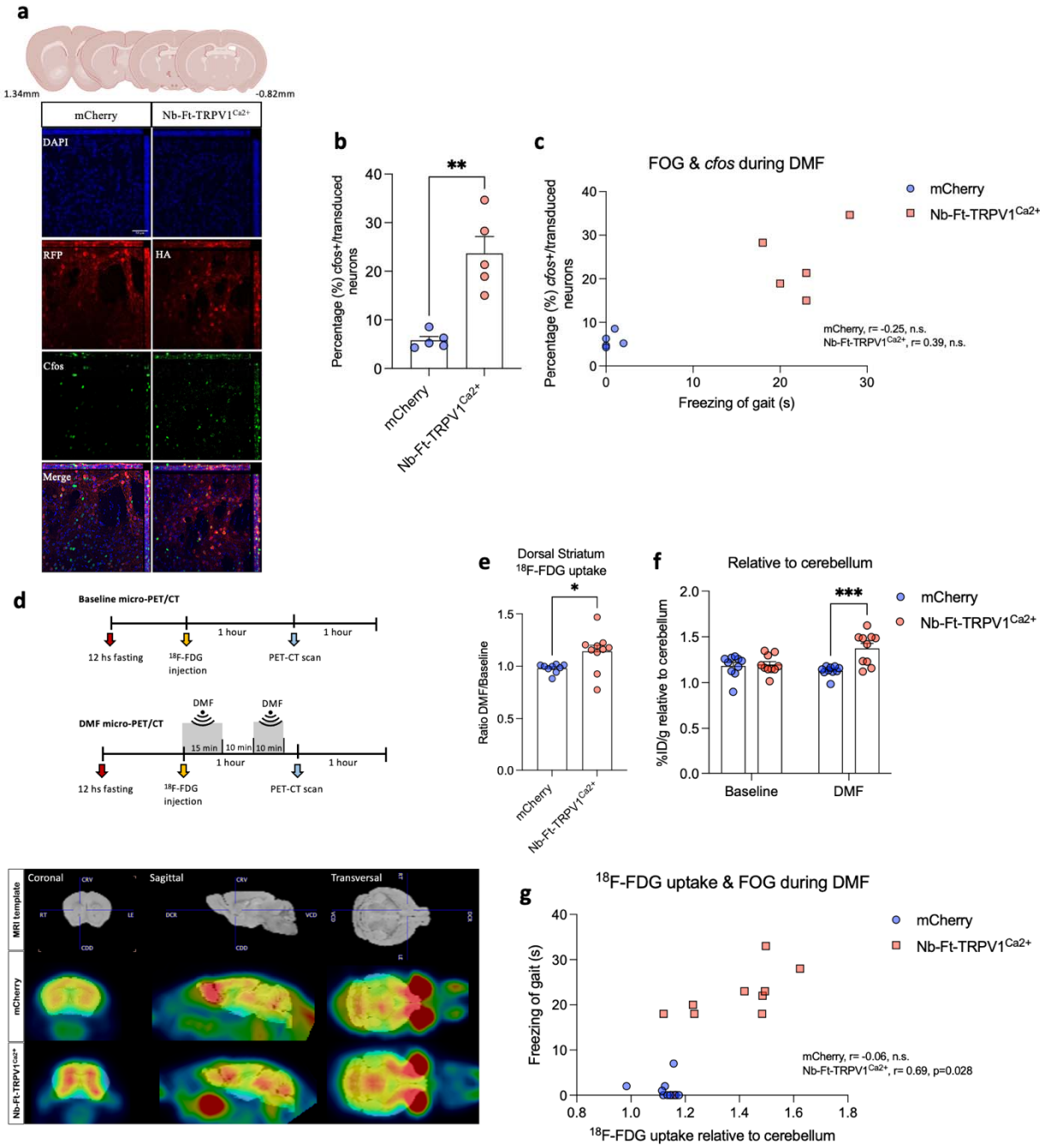

Fig. 3. Nb-Ft-TRPV1^{Ca2+} increases *c-fos* expression and cerebral metabolism upon DMF treatment. a. Immunostaining for *c-fos* (cyan) and HA or RFP (red) of dorsal striatum of A2a-Cre mice euthanized 1 hour following 15 minutes of DMF exposure. **b.** Percentage (%) of *c-fos* positive (+) neurons over total number of iSPNs expressing HA or RFP (n=5 mice per group/3

sections per mice). **c.** Correlation between *c-fos* expression and freezing of gait during DMF exposure (n=5 mice per group). **d.** Protocol and schema for 18-FDG micro-PET/CT scans procedure and analysis with representative micro-PET/CT imaging of A2a-Cre mouse brains expressing the Nb-Ft-TRPV1^{Ca2+} or the mCherry control virus following DMF exposure. 18-FDG uptake in dorsal striatum calculated as the percentage of injected dose/weight (%ID/g), **e.** DMF over baseline ratio. **f.** DMF over baseline normalized to cerebellum, in mCherry (blue bars/dots, n=8) and Nb-Ft-TRPV1^{Ca2+} (red bars/dots, n=8) mice. **g.** Correlation between DMF over baseline 18-FDG uptake ratio and freezing of gait during DMF exposure (n=10). Error bars show SEM. * represents p value < 0.05, ** represents p value < 0.001 with Student's t test. Anti-HA staining to detect Nb-Ft-TRVP1^{Ca2+} expression, anti-RFP staining to detect mCherry expression.

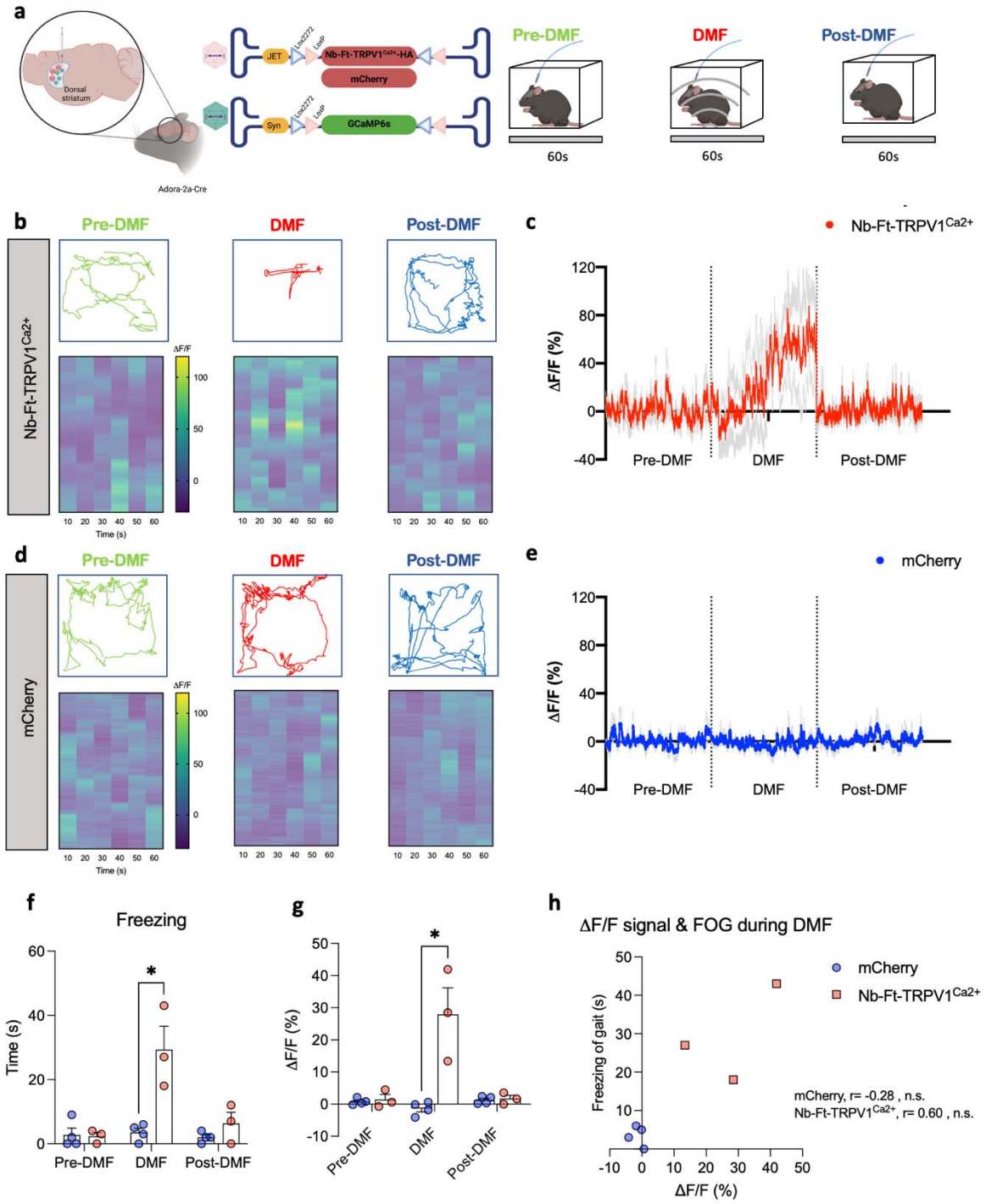

Fig. 4. Nb-Ft-TRPV1^{Ca2+} increases calcium transients in dorsal striatum. a. Schema of the double-floxed Cre-dependent AAV vector expressing the Nb-Ft-TRPV1^{Ca2+} or mCherry under the control of the JET promoter (red) combined with double floxed Cre-dependent AAV vector expressing GCaMP6s under the control of the Syn promoter (green). Behavioral methodology to

assess calcium transients during pre-DMF (green), DMF (red), and post-DMF (blue) treatment. **b.** Activity trace example of altered motor activity during bilateral striatal pre-DMF (green), DMF (red), and post-DMF (blue) stimulation in an Nb-Ft-TRPV1^{Ca2+} mouse with heatmap of GCaMP fluorescence aligned to pre-DMF (left), DMF (middle), and post-DMF (right) of the same animal shown in activity trace example expressing the Nb-Ft-TRPV1^{Ca2+} vector. **c.** Mean fluorescence aligned to pre-DMF, DMF, and post-DMF in Nb-Ft-TRPV1^{Ca2+} group (n=3). **d.** Activity trace example of altered motor activity during bilateral striatal pre-DMF (green), DMF (red), and post-DMF (blue) stimulation in an mCherry mouse with heatmap of GCaMP fluorescence aligned to pre-DMF (left), DMF (middle), and post-DMF (right) for the same animal shown in activity trace example expressing the mCherry vector. **e.** Mean fluorescence aligned to pre-DMF, DMF, and post-DMF in the mCherry group (n=4) **f.** Freezing of gait (FOG), **g.** Average delta (Δ) F/F (%) during pre-DMF, DMF, and post-DMF stimulation. **h.** Correlation between ΔF/F (%) calcium transients and FOG during DMF treatment. Error bars show SEM. * represents p value < 0.05 with Student's t test.

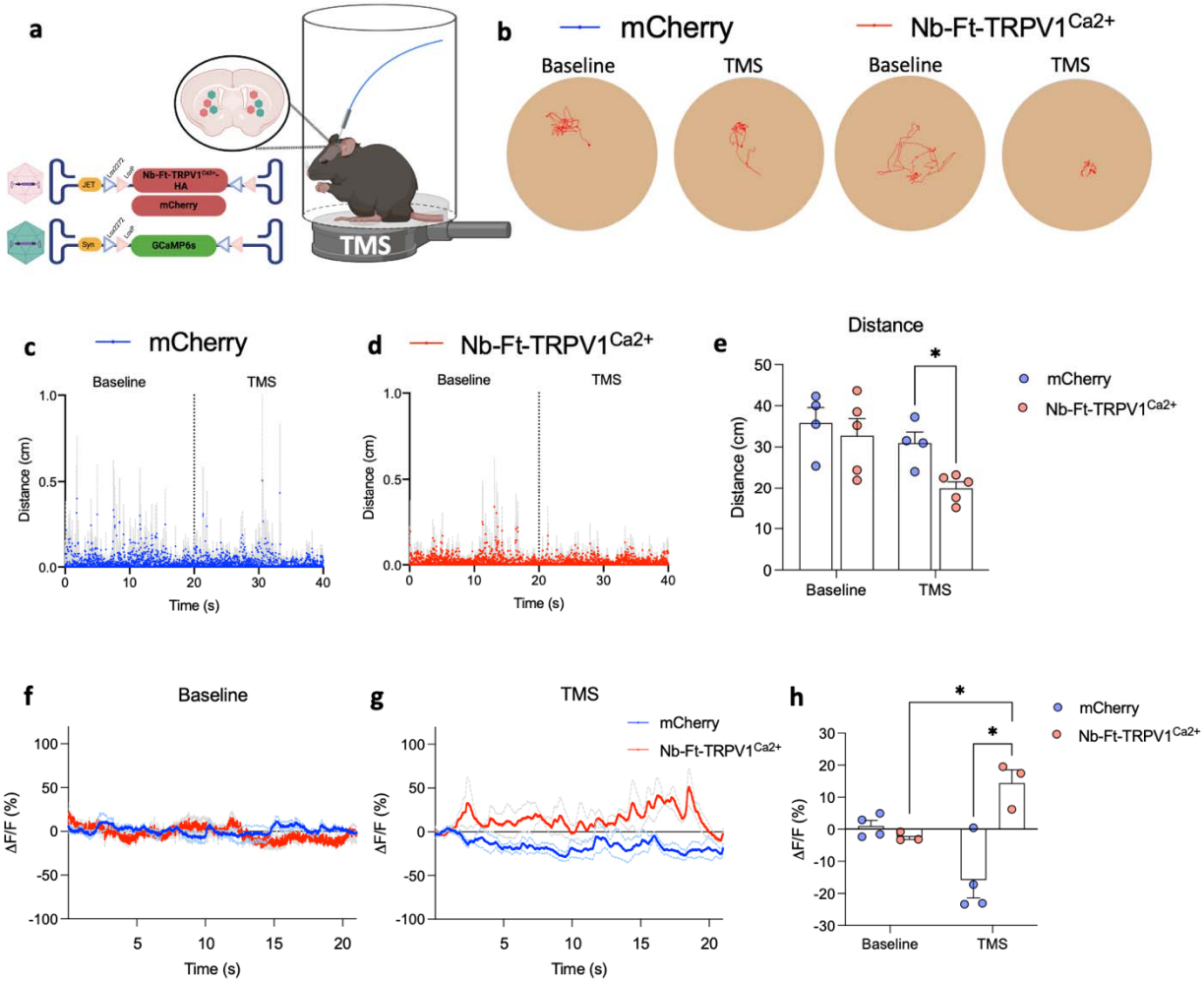

Fig. 5. Transcranial magnetic stimulation (TMS) treatment increases Nb-Ft-TRPV1^{Ca2+} mediated motor freezing and calcium transients in dorsal striatum. a. Schema of the TMS set up and A2a-Cre mice with bilateral injection of the double-floxed Cre-dependent AAV vector expressing the Nb-Ft-TRPV1^{Ca2+} or mCherry under the control of the JET promoter (red) combined with double floxed Cre-dependent AAV vector expressing GCaMP6s under the control of the Syn promoter (green) in dorsal striatum. **b.** Activity trace example of altered motor activity during baseline (left) and TMS (right) treatment in an mCherry mouse (blue), and Nb-Ft-TRPV1^{Ca2+} mouse (red). Distance ambulated during baseline (left) and TMS (right)

treatment in the **c.** mCherry group (blue), and **d.** Nb-Ft-TRPV1^{Ca2+} group (red). (n=4-5; data presented as the mean ± SEM in grey.). **e.** Average distance during baseline and TMS treatment in mCherry (blue) and Nb-Ft-TRPV1^{Ca2+} groups. **f.** Mean fluorescence during baseline in Nb-Ft-TRPV1^{Ca2+} (red) and mCherry (blue) mice (n=3; data presented as the mean ± SEM). **g.** Mean fluorescence during 20 seconds of TMS triggers every 2 seconds in Nb-Ft-TRPV1^{Ca2+} (red) and mCherry (blue) mice (n=3-4; data presented as the mean ± SEM). **h.** Grouped bar graph of Nb-Ft-TRPV1^{Ca2+} (red) and mCherry (blue) mice during baseline, and 20 seconds of TMS triggers every 2 seconds (n=3-4). Error bars show SEM. * represents p value < 0.05 with Student's t test.

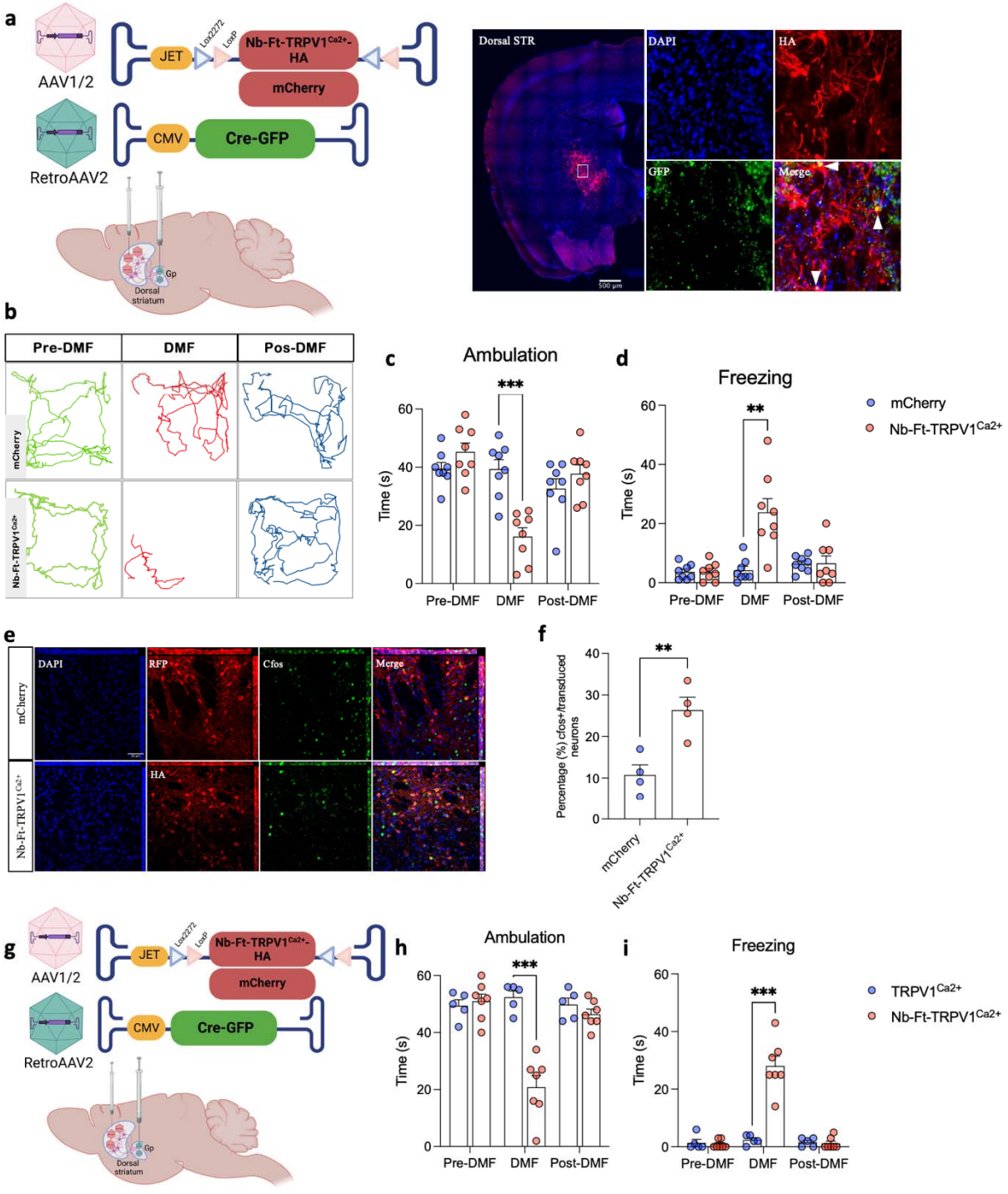

Fig. 6. Selective viral-mediated expression of Nb-Ft-TRPV1^{Ca2+} in the striatopallidal pathway elicit parkinsonian motor behavior in wild type mice. a. Schema of the double-floxed Cre-

dependent AAV vector expressing the Nb-Ft-TRPV1^{Ca2+} or mCherry under the control of the JET promoter in striatal iSPN projecting to the Gp achieved by Gp injection of a retrograde AAV2 vector carrying Cre-GFP, and immunostaining for GFP (green), HA (red) in wt mice demonstrates selective expression of the AAV- Nb-Ft-TRPV1^{Ca2+} in dorsal striatum iSPN projecting to the Gpe, white arrows show colocalization of GFP with HA. **b.** Example of altered motor activity during bilateral striatopallidal pre-DMF (green), DMF (red) and post-DMF (blue) stimulation, lines represent the mouse's path. Effect of DMF stimulation on **c.** Ambulation bout duration, and **d.** Freezing of gait in mCherry (blue bars/dots, n=8) and Nb-Ft-TRPV1^{Ca2+} (red bars/dots, n=8) mice. **e.** Immunostaining for *c-fos* (cyan) and HA (Nb-Ft-TRVP1^{Ca2+}; red) or RFP (mCherry; red) of dorsal striatum of wt mice euthanized 1 hour following 15 minutes of DMF exposure. White arrows show co-localization. **f.** Percentage (%) of *c-fos* positive (+) neurons over total number of iSPNs expressing HA or RFP (n=3 mice per group/3 sections per mice). **g.** Schema of the double-floxed Cre-dependent AAV vector expressing the Nb-Ft-TRPV1^{Ca2+} or TRPV1^{Ca2+} under the control of the JET promoter in striatal iSPNs projecting to the Gp achieved by Gp injection of a retrograde AAV2 vector carrying Cre-GFP. Effect of DMF stimulation on **h.** Ambulation bout duration, and **i.** Freezing of gait in TRPV1^{Ca2+} (blue bars/dots, n=5) and Nb-Ft-TRPV1^{Ca2+} (red bars/dots, n=7) mice. Error bars show SEM. ** represents p value < 0.001 with Student's t test.

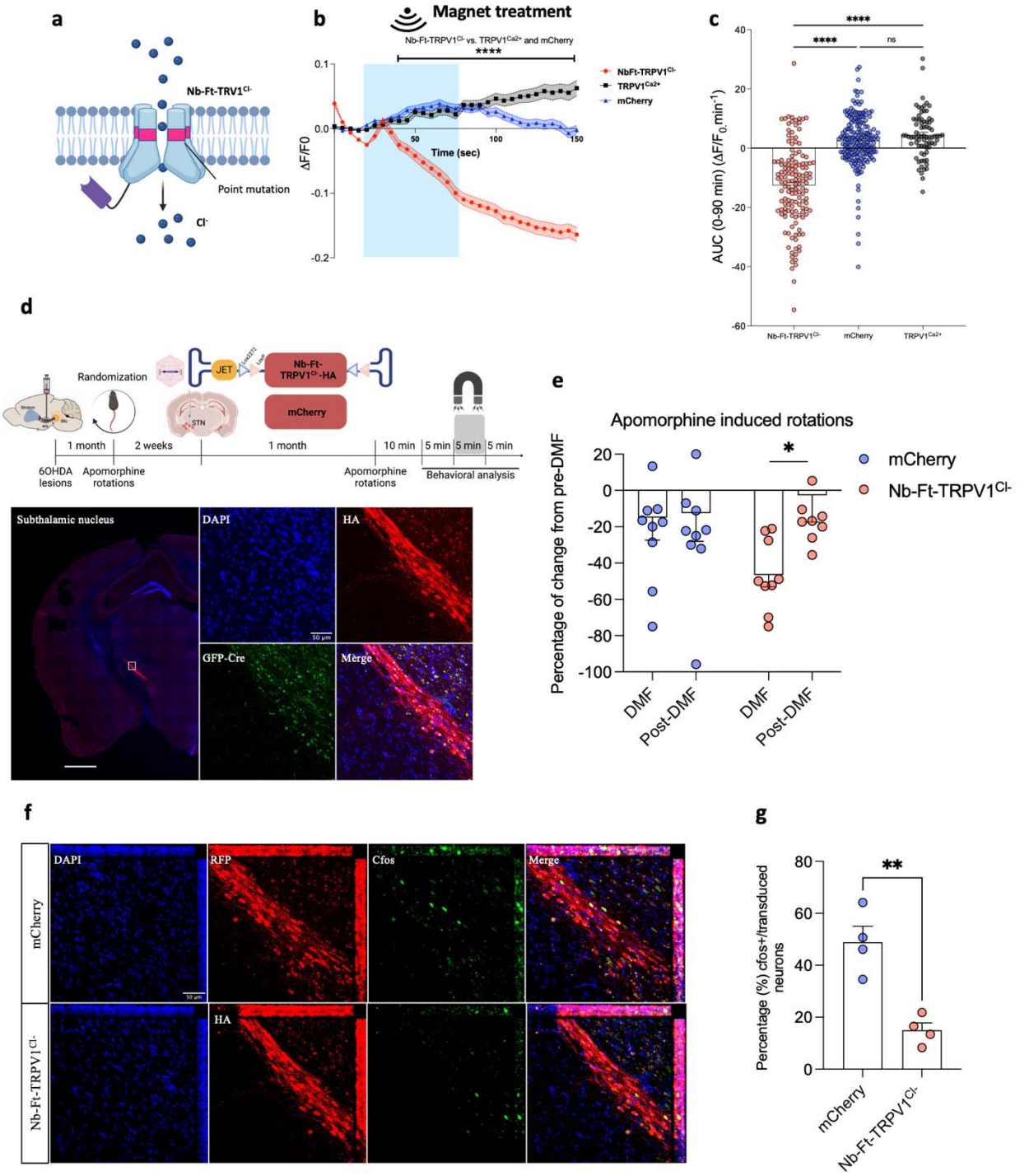

Fig. 7. Mutant Nb-Ft-TRPV1^{Cl-} inhibits neuronal activity of subthalamic nucleus projection neurons and rescues motor impairment in parkinsonian mice. a. Schema of inhibition system

with mutant Nb-Ft-TRPV1^{Cl-} membrane channel. **b.** Normalized change in MQAE fluorescence Intensity (ΔF/F0) of Neuro2A cells expressing mCherry, TRPV1^{Ca2+} or Nb-Ft-TRPV1^{Cl-} with low AMF application *in vitro*. **c.** AUC analysis of chloride imaging for Nb-Ft-TRPV1^{Cl-} channel. **d.** Protocol and schema for generation of parkinsonian PitX-2-Cre mice with unilateral injection of 6 hydroxydopamine (6-OHDA) in the medial forebrain bundle (MFB), followed by randomization based contralateral rotations induced by i.p. administration of apomorphine (0.25mg/kg) and ipsilateral intracranial injection of the double-floxed Cre-dependent AAV vector expressing the mutant Nb-Ft-TRPV1^{Cl-} under the control of the JET promoter in the subthalamic nucleus (STN). Representative immunostaining of the selective expression of Nb-Ft-TRPV1^{Cl-} (red) in STN neurons expressing Cre recombinase (Green). **e.** Percentage of change from pre-DMF treatment in contralateral rotations induced with apomorphine (0.25mg/kg, i.p.) in parkinsonian PitX-2-Cre mice expressing the Nb-Ft-TRPV1^{Cl-} or the mCherry control viruses in the STN during DMF, and post-DMF. **f.** Immunostaining for *c-fos* (cyan) and HA or mCherry (red) of STN of PiX-2-Cre mice euthanized 1 hour following 15 minutes of DMF exposure with apomorphine induced rotations (0.25mg/kg). White arrows show co-localization. **g.** Percentage (%) of *c-fos* positive (+) neurons over total number of iSPNs expressing HA or RFP (n=4 mice per group/3 sections per mice). Error bars show SEM. * represents p value < 0.05 with Student's t test. Anti-HA staining to detect Nb-Ft-TRVP1^{Ca2+} expression, anti-RFP staining to detect mCherry expression.